Beam-energy-dependent two-pion interferometry and the freeze-out eccentricity of pions measured in heavy ion collisions at the STAR detector

Beam-energy-dependent two-pion interferometry and the freeze-out eccentricity of pions measured in heavy ion collisions at the STAR detector

L. Adamczyk,[1] J. K. Adkins,[23] G. Agakishiev,[21] M. M. Aggarwal,[35] Z. Ahammed,[54] I. Alekseev,[19] J. Alford,[22] C. D. Anson,[32] A. Aparin,[21] D. Arkhipkin,[4] E. C. Aschenauer,[4] G. S. Averichev,[21] A. Banerjee,[54] D. R. Beavis,[4] R. Bellwied,[50] A. Bhasin,[20] A. K. Bhati,[35] P. Bhattarai,[49] H. Bichsel,[56] J. Bielcik,[13] J. Bielcikova,[14] L. C. Bland,[4] I. G. Bordyuzhin,[19] W. Borowski,[46] J. Bouchet,[22] A. V. Brandin,[30] S. G. Brovko,[6] S. Bültmann,[33] I. Bunzarov,[21] T. P. Burton,[4] J. Butterworth,[42] H. Caines,[58] M. Calderón de la Barca Sánchez,[6] D. Cebra,[6] R. Cendejas,[36] M. C. Cervantes,[48] P. Chaloupka,[13] Z. Chang,[48] S. Chattopadhyay,[54] H. F. Chen,[43] J. H. Chen,[45] L. Chen,[9] J. Cheng,[51] M. Cherney,[12] A. Chikanian,[58] W. Christie,[4] J. Chwastowski,[37] M. J. M. Codrington,[49] G. Contin,[26] J. G. Cramer,[56] H. J. Crawford,[5] X. Cui,[43] S. Das,[16] A. Davila Leyva,[49] L. C. De Silva,[12] R. R. Debbe,[4] T. G. Dedovich,[21] J. Deng,[44] A. A. Derevschikov,[38] R. Derradi de Souza,[8] S. Dhamija,[18] B. di Ruzza,[4] L. Didenko,[4] C. Dilks,[36] F. Ding,[6] P. Djawotho,[48] X. Dong,[26] J. L. Drachenberg,[53] J. E. Draper,[6] C. M. Du,[25] L. E. Dunkelberger,[7] J. C. Dunlop,[4] L. G. Efimov,[21] J. Engelage,[5] K. S. Engle,[52] G. Eppley,[42] L. Eun,[26] O. Evdokimov,[10] O. Eyser,[4] R. Fatemi,[23] S. Fazio,[4] J. Fedorisin,[21] P. Filip,[21] E. Finch,[58] Y. Fisyak,[4] C. E. Flores,[6] C. A. Gagliardi,[48] D. R. Gangadharan,[32] D. Garand,[39] F. Geurts,[42] A. Gibson,[53] M. Girard,[55] S. Gliske,[2] L. Greiner,[26] D. Grosnick,[53] D. S. Gunarathne,[47] Y. Guo,[43] A. Gupta,[20] S. Gupta,[20] W. Guryn,[4] B. Haag,[6] A. Hamed,[48] L-X. Han,[45] R. Haque,[31] J. W. Harris,[58] S. Heppelmann,[36] A. Hirsch,[39] G. W. Hoffmann,[49] D. J. Hofman,[10] S. Horvat,[58] B. Huang,[4] H. Z. Huang,[7] X. Huang,[51] P. Huck,[9] T. J. Humanic,[32] G. Igo,[7] W. W. Jacobs,[18] H. Jang,[24] E. G. Judd,[5] S. Kabana,[46] D. Kalinkin,[19] K. Kang,[51] K. Kauder,[10] H. W. Ke,[4] D. Keane,[22] A. Kechechyan,[21] A. Kesich,[6] Z. H. Khan,[10] D. P. Kikola,[55] I. Kisel,[15] A. Kisiel,[55] D. D. Koetke,[53] T. Kollegger,[15] J. Konzer,[39] I. Koralt,[33] L. K. Kosarzewski,[55] L. Kotchenda,[30] A. F. Kraishan,[47] P. Kravtsov,[30] K. Krueger,[2] I. Kulakov,[15] L. Kumar,[31] R. A. Kycia,[11] M. A. C. Lamont,[4] J. M. Landgraf,[4] K. D. Landry,[7] J. Lauret,[4] A. Lebedev,[4] R. Lednicky,[21] J. H. Lee,[4] M. J. LeVine,[4] C. Li,[43] W. Li,[45] X. Li,[39] X. Li,[47] Y. Li,[51] Z. M. Li,[9] M. A. Lisa,[32] F. Liu,[9] T. Ljubicic,[4] W. J. Llope,[42] M. Lomnitz,[22] R. S. Longacre,[4] X. Luo,[9] G. L. Ma,[45] Y. G. Ma,[45] D. M. M. D. Madagodagettige Don,[12] D. P. Mahapatra,[16] R. Majka,[58] S. Margetis,[22] C. Markert,[49] H. Masui,[26] H. S. Matis,[26] D. McDonald,[50] T. S. McShane,[12] N. G. Minaev,[38] S. Mioduszewski,[48] B. Mohanty,[31] M. M. Mondal,[48] D. A. Morozov,[38] M. K. Mustafa,[26] B. K. Nandi,[17] Md. Nasim,[31] T. K. Nayak,[54] J. M. Nelson,[3] G. Nigmatkulov,[30] L. V. Nogach,[38] S. Y. Noh,[24] J. Novak,[29] S. B. Nurushev,[38] G. Odyniec,[26] A. Ogawa,[4] K. Oh,[40] A. Ohlson,[58] V. Okorokov,[30] E. W. Oldag,[49] D. L. Olvitt, Jr.,[47] M. Pachr,[13] B. S. Page,[18] S. K. Pal,[54] Y. X. Pan,[7] Y. Pandit,[10] Y. Panebratsev,[21] T. Pawlak,[55] B. Pawlik,[34] H. Pei,[9] C. Perkins,[5] W. Peryt,[55] P. Pile,[4] M. Planinic,[59] J. Pluta,[55] N. Poljak,[59] K. Poniatowska,[55] J. Porter,[26] A. M. Poskanzer,[26] N. K. Pruthi,[35] M. Przybycien,[1] P. R. Pujahari,[17] J. Putschke,[57] H. Qiu,[26] A. Quintero,[22] S. Ramachandran,[23] R. Raniwala,[41] S. Raniwala,[41] R. L. Ray,[49] C. K. Riley,[58] H. G. Ritter,[26] J. B. Roberts,[42] O. V. Rogachevskiy,[21] J. L. Romero,[6] J. F. Ross,[12] A. Roy,[54] L. Ruan,[4] J. Rusnak,[14] O. Rusnakova,[13] N. R. Sahoo,[48] P. K. Sahu,[16] I. Sakrejda,[26] S. Salur,[26] J. Sandweiss,[58] E. Sangaline,[6] A. Sarkar,[17] J. Schambach,[49] R. P. Scharenberg,[39] A. M. Schmah,[26] W. B. Schmidke,[4] N. Schmitz,[28] J. Seger,[12] P. Seyboth,[28] N. Shah,[7] E. Shahaliev,[21] P. V. Shanmuganathan,[22] M. Shao,[43] B. Sharma,[35] W. Q. Shen,[45] S. S. Shi,[26] Q. Y. Shou,[45] E. P. Sichtermann,[26] R. N. Singaraju,[54] M. J. Skoby,[18] D. Smirnov,[4] N. Smirnov,[58] D. Solanki,[41] P. Sorensen,[4] H. M. Spinka,[2] B. Srivastava,[39] T. D. S. Stanislaus,[53] J. R. Stevens,[27] R. Stock,[15] M. Strikhanov,[30] B. Stringfellow,[39] M. Sumbera,[14] X. Sun,[26] X. M. Sun,[26] Y. Sun,[43] Z. Sun,[25] B. Surrow,[47] D. N. Svirida,[19] T. J. M. Symons,[26] M. A. Szelezniak,[26] J. Takahashi,[8] A. H. Tang,[4] Z. Tang,[43] T. Tarnowsky,[29] J. H. Thomas,[26] A. R. Timmins,[50] D. Tlusty,[14] M. Tokarev,[21] S. Trentalange,[7] R. E. Tribble,[48] P. Tribedy,[54] B. A. Trzeciak,[13] O. D. Tsai,[7] J. Turnau,[34] T. Ullrich,[4] D. G. Underwood,[2] G. Van Buren,[4] G. van Nieuwenhuizen,[27] M. Vandenbroucke,[47] J. A. Vanfossen, Jr.,[22] R. Varma,[17] G. M. S. Vasconcelos,[8] A. N. Vasiliev,[38] R. Vertesi,[14] F. Videbæk,[4] Y. P. Viyogi,[54] S. Vokal,[21] A. Vossen,[18] M. Wada,[49] F. Wang,[39] G. Wang,[7] H. Wang,[4] J. S. Wang,[25] X. L. Wang,[43] Y. Wang,[51] Y. Wang,[10] G. Webb,[23] J. C. Webb,[4] G. D. Westfall,[29] H. Wieman,[26] S. W. Wissink,[18] R. Witt,[52] Y. F. Wu,[9] Z. Xiao,[51] W. Xie,[39] K. Xin,[42] H. Xu,[25] J. Xu,[9] N. Xu,[26] Q. H. Xu,[44] Y. Xu,[43] Z. Xu,[4] W. Yan,[51] C. Yang,[43] Y. Yang,[25] Y. Yang,[9] Z. Ye,[10] P. Yepes,[42] L. Yi,[39] K. Yip,[4] I-K. Yoo,[40] N. Yu,[9] Y. Zawisza,[43] H. Zbroszczyk,[55] W. Zha,[43] J. B. Zhang,[9] J. L. Zhang,[44] S. Zhang,[45] X. P. Zhang,[51] Y. Zhang,[43] Z. P. Zhang,[43] F. Zhao,[7] J. Zhao,[9] C. Zhong,[45] X. Zhu,[51] Y. H. Zhu,[45] Y. Zoulkarneeva,[21] and M. Zyzak[15]

(STAR Collaboration)

[1]*AGH University of Science and Technology, Cracow, Poland*
[2]*Argonne National Laboratory, Argonne, Illinois 60439, USA*
[3]*University of Birmingham, Birmingham, United Kingdom*
[4]*Brookhaven National Laboratory, Upton, New York 11973, USA*
[5]*University of California, Berkeley, California 94720, USA*
[6]*University of California, Davis, California 95616, USA*
[7]*University of California, Los Angeles, California 90095, USA*
[8]*Universidade Estadual de Campinas, Sao Paulo, Brazil*
[9]*Central China Normal University (HZNU), Wuhan 430079, China*
[10]*University of Illinois at Chicago, Chicago, Illinois 60607, USA*
[11]*Cracow University of Technology, Cracow, Poland*

[12]*Creighton University, Omaha, Nebraska 68178, USA*
[13]*Czech Technical University in Prague, FNSPE, Prague 115 19, Czech Republic*
[14]*Nuclear Physics Institute AS CR, 250 68 Řež/Prague, Czech Republic*
[15]*Frankfurt Institute for Advanced Studies FIAS, Germany*
[16]*Institute of Physics, Bhubaneswar 751005, India*
[17]*Indian Institute of Technology, Mumbai, India*
[18]*Indiana University, Bloomington, Indiana 47408, USA*
[19]*Alikhanov Institute for Theoretical and Experimental Physics, Moscow, Russia*
[20]*University of Jammu, Jammu 180001, India*
[21]*Joint Institute for Nuclear Research, Dubna 141 980, Russia*
[22]*Kent State University, Kent, Ohio 44242, USA*
[23]*University of Kentucky, Lexington, Kentucky 40506-0055, USA*
[24]*Korea Institute of Science and Technology Information, Daejeon, Korea*
[25]*Institute of Modern Physics, Lanzhou, China*
[26]*Lawrence Berkeley National Laboratory, Berkeley, California 94720, USA*
[27]*Massachusetts Institute of Technology, Cambridge, Massachusetts 02139-4307, USA*
[28]*Max-Planck-Institut für Physik, Munich, Germany*
[29]*Michigan State University, East Lansing, Michigan 48824, USA*
[30]*Moscow Engineering Physics Institute, Moscow, Russia*
[31]*National Institute of Science Education and Research, Bhubaneswar 751005, India*
[32]*Ohio State University, Columbus, Ohio 43210, USA*
[33]*Old Dominion University, Norfolk, Virginia 23529, USA*
[34]*Institute of Nuclear Physics PAN, Cracow, Poland*
[35]*Panjab University, Chandigarh 160014, India*
[36]*Pennsylvania State University, University Park, Pennsylvania 16802, USA*
[37]*Institute of Nuclear Physics, Polish Academy of Sciences, PL-31342 Krakow, Poland*
[38]*Institute of High Energy Physics, Protvino, Russia*
[39]*Purdue University, West Lafayette, Indiana 47907, USA*
[40]*Pusan National University, Pusan, Republic of Korea*
[41]*University of Rajasthan, Jaipur 302004, India*
[42]*Rice University, Houston, Texas 77251, USA*
[43]*University of Science and Technology of China, Hefei 230026, China*
[44]*Shandong University, Jinan, Shandong 250100, China*
[45]*Shanghai Institute of Applied Physics, Shanghai 201800, China*
[46]*SUBATECH, Nantes, France*
[47]*Temple University, Philadelphia, Pennsylvania 19122, USA*
[48]*Texas A&M University, College Station, Texas 77843, USA*
[49]*University of Texas, Austin, Texas 78712, USA*
[50]*University of Houston, Houston, Texas 77204, USA*
[51]*Tsinghua University, Beijing 100084, China*
[52]*United States Naval Academy, Annapolis, Maryland 21402, USA*
[53]*Valparaiso University, Valparaiso, Indiana 46383, USA*
[54]*Variable Energy Cyclotron Centre, Kolkata 700064, India*
[55]*Warsaw University of Technology, Warsaw, Poland*
[56]*University of Washington, Seattle, Washington 98195, USA*
[57]*Wayne State University, Detroit, Michigan 48201, USA*
[58]*Yale University, New Haven, Connecticut 06520, USA*
[59]*University of Zagreb, Zagreb HR-10002, Croatia*
(Received 30 January 2015; published 10 July 2015)

We present results of analyses of two-pion interferometry in Au + Au collisions at $\sqrt{s_{NN}} = 7.7$, 11.5, 19.6, 27, 39, 62.4, and 200 GeV measured in the STAR detector as part of the BNL Relativistic Heavy Ion Collider Beam Energy Scan program. The extracted correlation lengths (Hanbury-Brown–Twiss radii) are studied as a function of beam energy, azimuthal angle relative to the reaction plane, centrality, and transverse mass (m_T) of the particles. The azimuthal analysis allows extraction of the eccentricity of the entire fireball at kinetic freeze-out. The energy dependence of this observable is expected to be sensitive to changes in the equation of state. A new global fit method is studied as an alternate method to directly measure the parameters in the azimuthal analysis.

The eccentricity shows a monotonic decrease with beam energy that is qualitatively consistent with the trend from all model predictions and quantitatively consistent with a hadronic transport model.

DOI: 10.1103/PhysRevC.92.014904 PACS number(s): 25.75.Gz, 25.75.Nq

I. INTRODUCTION

The Beam Energy Scan program performed at the BNL Relativistic Heavy Ion Collider (RHIC) in 2010 and 2011 was designed to map features expected to appear in the QCD phase diagram [1]. At the highest RHIC energies evidence suggests that the matter formed in heavy ion collisions is a hot, strongly coupled fluid of deconfined quarks and gluons (sQGP) [2–5], with rather low chemical potential, μ_B. The nature of this phase transition is likely a smooth, rapid cross-over transition [6–9]. As the beam energy is lowered, the matter produced near midrapidity evolves through regions of the phase diagram at larger μ_B. At higher chemical potentials there are predictions from lattice calculations of a change to a first-order phase transition with an associated latent heat [10–16] and a critical point at some intermediate chemical potential [17]. The relative amounts of time the matter spends in an sQGP, mixed or hadronic phase, may imprint a signal on observables that are sensitive to the equation of state [18]. It is important, therefore, to study such observables as a function of beam energy both to search for possible nonmonotonic behavior (which could indicate interesting physical changes in some aspect of the collisions) and to provide more stringent experimental guidance to theory and models. The sizes and shapes that describe the matter produced in the collisions at freeze-out provide just this type of observable [19].

Results of two-pion interferometry analyses [often referred to as Hanbury-Brown–Twiss (HBT) analyses] are presented in this paper as a function of beam energy. Hanbury Brown and Twiss invented the intensity interferometry technique to measure sizes of nearby stars [20]. The technique was extended to particle physics [21] to study angular distributions of pion pairs in $p\bar{p}$ annihilations, finding that quantum statistics caused an enhancement in pairs with low relative momentum. In subsequent HBT analyses the method has evolved into a precision tool for measuring space-time properties of the regions of homogeneity at kinetic freeze-out in heavy ion collisions [22]. Two-pion interferometry yields HBT radii that describe the geometry of these regions of homogeneity (regions that emit correlated pion pairs). The observation that HBT radii increase for more central collisions is attributed to the increasing volume of the source, an example of how HBT can probe spatial sizes and shapes [22]. In addition to the spatial shape and size of these regions from which particle pairs are emitted, space-momentum correlations induced by collective (and anisotropic) flow [23] may imprint patterns on the results. For instance, the HBT radii exhibit a systematic decrease with mean pair transverse momentum, k_T, which has been attributed to transverse and longitudinal flow [23,24]. The presence of flow induces space-momentum correlations so that the size of the regions emitting particles does not correspond to the entire fireball created in a collision [22–24]. In standard HBT analyses, integrated over azimuthal angle relative to the reaction plane, the extracted source sizes correspond only to some smaller region of the total volume; the higher the transverse momentum, k_T, the smaller the radii describing the volume emitting the particles [22]. However, in HBT analyses performed relative to the reaction plane, sinusoidal variations in the shape of these smaller source regions can be connected to the overall shape of the entire fireball [23,24].

Previous HBT analyses from various experiments have led to a large world data set for standard, nonazimuthal HBT results at the BNL Alternating Gradient Synchrotron (AGS) [25–27] and the CERN Super Proton Synchrotron (SPS) [28–31], as well as top RHIC energies [32–35] and at the CERN Large Hadron Collider (LHC) [36–38]. In contrast, only a few azimuthal HBT results have been reported previously by E895 [39], STAR [40], PHENIX [41], and CERES [42]. While the results suggested possible nonmonotonic behavior in the freeze-out shape of the collisions with a minimum appearing around a collision energy per nucleon of 17.3 GeV, the sparse amount of data coming from several different experiments could not allow one to draw a definite conclusion [42]. In this paper, the results of azimuthally integrated HBT analyses are placed in the context of the world data set reproducing the low-energy and high-energy results and filling in the intermediate energy region with results from a single detector and identical analysis techniques. The azimuthally differential HBT results are also presented across this wide range of energies allowing extraction of the beam energy dependence of the transverse eccentricity at freeze-out.

In the case of the azimuthally differential analysis, a new global fit method is developed. The technique, described in this paper, uses a Gaussian parametrization. However, several correlation functions constructed in azimuthal bins relative to the reaction plane are fit simultaneously. This allows direct extraction of Fourier coefficients that describe the observed sinusoidal variations in the shape of the regions of homogeneity that emit pion pairs. This technique avoids correlated errors that arise from a correction for finite-bin-width and event-plane resolution effects and it is more robust in some cases where statistics and event-plane resolutions are low. The global fit method provides the most reliable estimate of the shape of the fireball at kinetic freeze-out, which, as described in the next section, is used to search for a change in the type of phase transition at lower energies. The experimental results of this study are presented in Sec. VI B 3.

II. COLLISION EVOLUTION AND FREEZE-OUT SHAPE

A primary theme explored in this analysis is the connection between the type of phase transition the system experiences and the shape of the collision during kinetic freeze-out. Therefore, in this section we explore the relationship between the underlying physics and the final shape achieved in the collisions. In noncentral collisions, the second-order anisotropy of the participant zone (in the transverse plane) is an ellipse extended out of the reaction plane (the plane containing the

impact parameter and beam direction). Initial-state fluctuations in positions of participant nucleons may cause deviations from a precise elliptical shape [43]. Nevertheless, the initial shape is approximately elliptical and can be estimated using Monte Carlo Glauber calculations. Owing to the anisotropic shape and the speed of sound, $c_s^2 = \partial p/\partial e$ (where p is pressure and e is energy density), larger initial pressure gradients appear along the short axis. These stronger in-plane pressure gradients drive preferential in-plane expansion, thereby reducing the eccentricity. The system must evolve to a less out-of-plane extended freeze-out shape. Longer lifetimes, stronger pressure gradients, or both, would lead to expansion to an even more round or even in-plane extended (negative eccentricity) shape at kinetic freeze-out. It would be expected that increasing the beam energy would lead to longer lifetimes and pressure gradients and so a monotonically decreasing excitation function for the freeze-out eccentricity would be expected [19]. In fact, all transport and hydrodynamic models predict a monotonic decrease in the energy ranges studied here.

There is, however, another consideration related to the equation of state. If the nature of the phase transition changes from a smooth crossover at high energy to a first-order transition at lower energy, the matter will evolve through a mixed-phase regime (associated with a latent heat) during which the pressure gradients vanish ($c_s^2 = 0$). Outside of a mixed-phase regime, the equation of state has even stronger pressure gradients ($c_s^2 = 1/3$) in the sQGP phase than the hadronic phase ($c_s^2 = 1/6$) [44,45]. As the collision energy is varied, the collisions evolve along different trajectories through the T-μ_B phase diagram. At low energy the system may evolve through a first-order phase transition and the length of time spent in the various phases may alter the amount of expansion that takes place prior to freeze-out [45]. It is possible that a nonmonotonic freeze-out shape might be observed as a result. In fact, it was speculated in Ref. [19] that the possible minimum observed in the previously available freeze-out eccentricity measurements might be caused by entrance into a mixed-phase regime around a minimum, followed by a maximum at higher energy above which the system achieves complete deconfinement (and the strong pressure gradients reappear). Measuring the energy dependence of the freeze-out shape therefore allows one to probe interesting physics related to both the equation of state and the dynamical processes that drive the evolution of the collisions.

III. EXPERIMENTAL SETUP AND EVENT, TRACK, AND PAIR SELECTIONS

A. STAR detector

The STAR detector [46] was used to reconstruct Au + Au collisions provided at $\sqrt{s_{NN}} = 7.7$, 11.5, 19.6, 27, 39, 62.4, and 200 GeV as part of a first phase of the Beam Energy Scan program. The main detector used in this analysis is the Time Projection Chamber (TPC) [47,48], which allows reconstruction of the momentum of charged particles used for event-plane determination, including the charged pions used in the HBT analyses. The TPC covers the pseudorapidity range $|\eta| < 1$ and has full 2π azimuthal acceptance. It is located inside a 0.5-T solenoidal magnetic field for all energies to aid in identifying the charge, momentum, and species of each track. Zero-degree calorimeters, beam-beam counters, and/or vertex position detectors, located at large rapidities near the beamline, were tuned online to collect high statistics, minimum-bias data sets at each energy. Measuring coincidences of spectator particles in the subsystems allows selection of collisions that occur near the center of the detector.

TABLE I. Number of analyzed events and z-vertex range, V_Z, at each energy.

$\sqrt{s_{NN}}$ (GeV)	$\lvert V_Z\rvert$ (cm)	N_{events} (10^6)
7.7	<70	3.9
11.5	<50	10.7
19.6	<30	15.4
27	<30	30.8
39	<30	8.8
62.4	<30	10.1
200	<30	11.6

B. Event selection

Events included in the analysis were selected using the reconstructed vertex position. The radial vertex position ($V_R = \sqrt{V_X^2 + V_Y^2}$) was required to be less than 2 cm to reject collisions with the beam pipe. The vertex position along the beam direction, V_Z, was required to be near the center of the detector as summarized in Table I, with larger ranges at 7.7 and 11.5 GeV to maximize statistics. The number of events at each energy used in this analysis are also listed in Table I.

The events were binned in different centrality ranges based on multiplicity as described in Ref. [49]. For the azimuthal HBT analysis, data in the 0%–5%, 5%–10%, 10%–20%, 20%–30%, and 30%–40% centrality bins were used. For the nonazimuthal HBT analysis, additional 40%–50%, 50%–60%, and 60%–70% bins were also studied.

C. Particle selection

Tracks were selected in three rapidity ranges: $-1 < y < -0.5$ (backward rapidity), $-0.5 < y < 0.5$ (midrapidity), and $0.5 < y < 1$ (forward rapidity). Each track was required to have hits on more than 15 (out of 45 maximum) of the rows of TPC readout pads to ensure good tracks. A requirement on the distance of closest approach (D_{CA}) to the primary vertex, $D_{\text{CA}} < 3$ cm, was imposed to reduce contributions from nonprimary pions.

Particle identification is accomplished by measuring energy loss in the gas, dE/dx, for each track and comparing to the expected value for each species ($i = e^{\pm}, \pi^{\pm}, k^{\pm}, p, \bar{p}$) using the equation

$$n\sigma_i = \frac{1}{\sigma_i} \ln\left(\frac{dE/dx_{\text{measured}}}{dE/dx_{\text{expected},i}}\right), \tag{1}$$

where σ_i is the dE/dx resolution of the TPC. Tracks with $|n\sigma_\pi| < 2$ allow identification of pions for use in the analysis. An additional requirement is that $|n\sigma_e|$, $|n\sigma_k|$, and $|n\sigma_p| > 2$

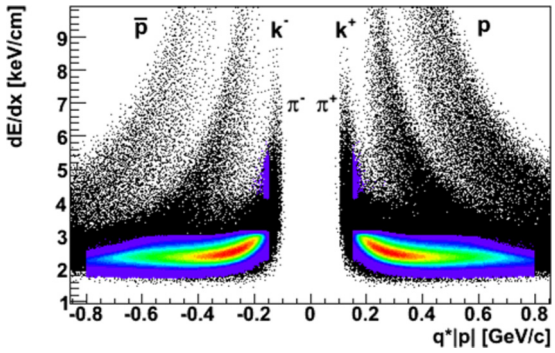

FIG. 1. (Color online) The energy loss in the TPC, dE/dx. The colored region highlights the pions selected for this analysis. The gaps in the colored region at $|p| \approx 0.2$ GeV/c are caused by the cut to eliminate electrons from the analysis in the region where the electron and pion bands overlap. This example is from 0%–5% central, 27-GeV Au + Au collisions.

suppress contamination from other particles. Additionally, a transverse momentum cut, $0.15 < p_T < 0.8$ GeV/c, further ensures particles come from the region where the pion band is separated from the kaon band. Any contamination is estimated to be less than 1.7%, even before the $n\sigma$ cut to reject kaons. Figure 1 demonstrates that these cuts effectively remove particles other than pions.

D. Pair k_T cuts and binning

Similar to previous analyses [33–35,40] pairs were required to have average transverse pair momenta, $k_T = |\vec{p}_{T1} + \vec{p}_{T2}|/2$, in the range $0.15 < k_T < 0.6$ GeV/c. For the nonazimuthal HBT analyses four k_T bins were used: [0.15,0.25], [0.25,0.35], [0.35,0.45], and [0.45,0.6] GeV/c. This binning allows the presentation of results as a function of mean k_T (or $m_T = \sqrt{k_T^2 + m_\pi^2}$) in each bin. These bins yield mean k_T values similar to those in the data from previous analyses allowing direct comparison of certain quantities to previously observed trends.

In earlier azimuthal HBT studies by CERES [42] and STAR [40] the analysis was performed in similar, narrow k_T bins. For an azimuthally differential HBT analysis the statistics are spread across at least four additional azimuthal bins. At the lowest energies this did not allow for sufficient statistics. For instance, the 7.7-GeV data set has both the fewest number of events and the lowest multiplicity per event in each centrality bin. Reliable results could not be obtained from data split into both multiple k_T and multiple bins relative to the reaction plane. Instead, a single k_T-integrated analysis was performed using all pairs in the combined range $0.15 < k_T < 0.6$ GeV/c, with $\langle k_T \rangle \approx 0.31$ GeV/c. The eccentricity at kinetic freeze-out exhibits a systematic decrease by as much as 0.02 when using a single wide k_T range compared to analyses where results from several narrow k_T ranges are averaged. This is simply because the lowest k_T bin appears to give a slightly smaller eccentricity. When a wide bin is used the results are biased toward the low k_T results owing to the much higher statistics of the low-k_T pairs. In the earlier analyses, CERES reported a weighted average of results for different k_T bins, while STAR used an average without statistical weights. In any case, to compare the present results as a function of $\sqrt{s_{NN}}$, the same k_T integrated range was used for all energies.

For the azimuthally differential analysis, the pairs were separated into four 45°-wide azimuthal bins relative to the reaction-plane direction using the angle $\Phi = \phi_{\text{pair}} - \psi_2$. The angle of each pair, ϕ_{pair}, is the azimuthal angle of the average pair transverse momentum vector, $\vec{k}_T$, and ψ_2 is the second-order event-plane angle defined in the range $[0,\pi]$. This allows measurement of the oscillations of parameters necessary to estimate the freeze-out eccentricity as projected on the transverse plane. A first-order analysis could provide additional information at the lowest energies [19,24]. However, significant additional work is needed to obtain first-order results owing to complications from relatively low statistics spread across more bins and with much lower first-order (compared to second order) event-plane resolutions.

IV. ANALYSIS METHOD

A. The correlation function

The experimental correlation function is constructed by forming the distributions of relative momenta, $\vec{q} = (\vec{p}_1 - \vec{p}_2)$. A numerator, $N(\vec{q})$, uses particles from the same event, while a mixed event denominator, $D(\vec{q})$, uses particles from different events. The numerator distribution is driven by two-particle phase-space, quantum statistics, and Coulomb interactions, while the denominator reflects only phase-space effects. Because quantum statistics and final-state interactions are driven by freeze-out geometry [22], the ratio

$$C(\vec{q}) = \frac{N(\vec{q})}{D(\vec{q})} \tag{2}$$

carries geometrical information. In the azimuthally differential analysis, four correlation functions were formed, corresponding to four 45°-wide angular bins relative to the event plane centered at 0° (in-plane), 45°, 90° (out-of-plane), and 135°. The angle between the transverse momentum for each pair and the event plane is used to assign each pair to one of the correlation functions. The denominators were constructed with pairs formed from mixed events. Events were mixed only with other events in the same centrality bin and with relative z vertex positions of less than 5 cm. For the azimuthally differential case, events were also required to have the estimated reaction plane within 22.5°, similar to an earlier analysis [40]. Reducing the width of the mixing bins only changes the relative normalizations in the different angular bins but has no effect on the other fit parameters. The correlation functions in this analysis are formed with like-sign pions and the separate distributions for $\pi^+\pi^+$ and $\pi^-\pi^-$ are later combined before fitting because no significant difference between the two cases has been observed.

Detector inefficiency and acceptance effects apply to both the numerator and the denominator and so, in taking the ratio to form the correlation function, these effects largely cancel. However, two-particle reconstruction inefficiencies

allow track splitting and merging effects which are removed, as will be described.

A single charged-particle track may be reconstructed as two tracks with nearly identical momentum by the tracking algorithm. This so-called track splitting can strongly affect correlation measurements by contributing false pairs to the correlation function at small relative momenta, the signal region. The same algorithm, described in Ref. [33], to remove split tracks is used in the current analysis. Studies analogous to those in Ref. [33] show the same "splitting level" requirement, $L_S < 0.6$, is also effective at removing track splitting effects in the current data sets.

However, two particles with small relative momenta can be reconstructed as a single track, thus reducing the measured number of correlated particles. In the following we briefly recapitulate the technique applied for removing track merging effects, detailed in Ref. [33]. If two tracks have hits on the same row of readout pads in the TPC that are too close together, they would appear as a single "merged" hit. Two tracks with such merged hits on many of the 45 rows of TPC readout pads are more likely to be reconstructed as a single merged track. For each pair of tracks, the fraction of hits that are close enough so they would appear merged is computed. The allowed fraction of merged hits ($F_{\rm MH}$) can be reduced until the effect is eliminated. The same algorithm can be applied to track pairs from the numerator and denominator. It was determined that $F_{\rm MH} < 10\%$ reduced track merging effects as much as possible. While this approach eliminates the potentially large effect of track merging, it introduces a systematic uncertainty owing to the non-Gaussianness of the correlation function. The azimuthal HBT analysis is more sensitive to the track merging cut and allows the systematic uncertainty associated with this requirement to be estimated in Sec. IV E. Studies analogous to those in Ref. [33] using current low-energy data sets lead to the same dependence of the radii on $F_{\rm MH}$, so in the present analyses the same requirement that $F_{\rm MH} < 10\%$ is imposed to remove effects of track merging.

B. Bertsch-Pratt parametrization

The relative pair momentum, $\vec{q}$, is projected onto the Bertsch-Pratt [50–52], out-side-long (or o-s-l), coordinate system so that $q_{\rm out}$ lies along the direction of the average transverse pair momentum, $\vec{k}_T$, while $q_{\rm long}$ lies along the "longitudinal" beam direction, and $q_{\rm side}$ is perpendicular to the other directions and is therefore also in the transverse plane. The relative momentum is expressed in the longitudinal comoving system (LCMS) in which the longitudinal component of the pair velocity vanishes.

To extract the bulk shape of the particle-emitting regions, a Gaussian parametrization is typically used:

$$C(\vec{q}) = (1-\lambda) + K_{\rm Coul}(q_{\rm inv})\lambda \exp\left(-q_{\rm o}^2 R_{\rm o}^2 - q_{\rm s}^2 R_{\rm s}^2 - q_{\rm l}^2 R_{\rm l}^2 - 2q_{\rm o}q_{\rm s}R_{\rm os}^2 - 2q_{\rm o}q_{\rm l}R_{\rm ol}^2\right). \quad (3)$$

The λ parameter accounts for nonprimary particles that may come from resonance decays and misidentified particles [33]. The parameter $R_{\rm ol}^2$ in Eq. (3) is relevant when analyzing rapidity slices not centered at midrapidity [53]. It was not used in Ref. [33], which focused exclusively on midrapidity pions. The values of $K_{\rm Coul}$ account for the Coulomb interaction as discussed in the next section. An overall normalization of the correlation function, also determined during the fitting procedure, scales the correlation function to a value of unity at large values of $|\vec{q}|$.

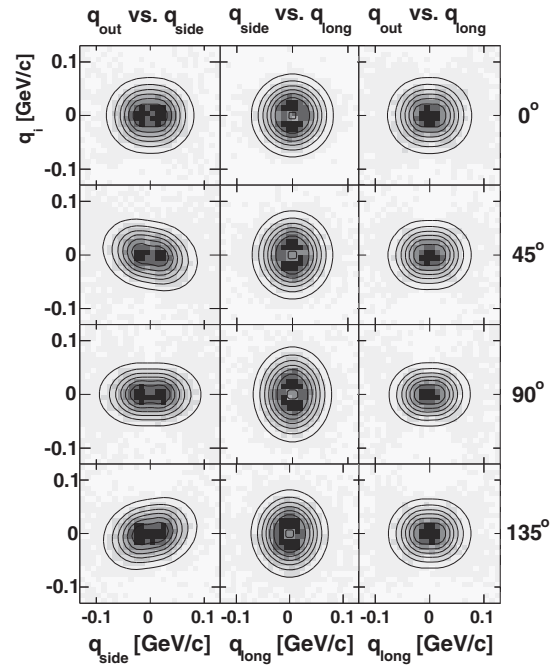

FIG. 2. Two-dimensional projections of a correlation function in the $q_{\rm o}$-$q_{\rm s}$, $q_{\rm s}$-$q_{\rm l}$, and $q_{\rm o}$-$q_{\rm l}$ planes for like-sign pions at midrapidity in 20%–30% central, 27-GeV collisions with $0.15 < k_T < 0.6$ GeV/c. All scales are in GeV/c. In each case the third component is projected over ± 0.03 GeV/c. The emission angles relative to the event plane are within $\pm 22.5^\circ$ of the bin centers indicated along the right side. The tilt in the $q_{\rm o}$-$q_{\rm s}$ plane is clearly visible. Contour lines represent projections of the corresponding fit.

The $R_{\rm ol}^2$ term vanishes at midrapidity, but becomes positive (negative) at forward (backward) rapidity in both azimuthal and nonazimuthal analyses [52]. For the azimuthally integrated analysis $R_{\rm os}^2$ vanishes, while in an azimuthally differential analysis a second-order sinusoidal variation appears relative to the reaction plane. Parametrically, a nonzero cross term corresponds to a tilt of the correlation function in $\vec{q}$ space. This can be seen clearly in Fig. 2 in the $q_{\rm out}$-$q_{\rm side}$ plane. At 45° there is a tilt resulting in a positive $R_{\rm os}^2$ cross term. At 135° there is an opposite tilt corresponding to a negative $R_{\rm os}^2$ cross term. The interplay between the cross terms and the inherent non-Gaussianness of the correlation function is discussed later in the Appendix, where folding the relative momentum distributions allows covariations in the fit parameters that would strongly affect the results. In this analysis, no folding of $\vec{q}$ space is performed, eliminating this effect.

In the azimuthally differential analysis, several correlation functions are constructed for different angular bins. These are each fit with Eq. (3) to extract the fit parameters. The relationship between these fit parameters describing the regions of homogeneity and the shape of the source region (the

collision fireball at kinetic freeze-out) has been described in several references, such as Refs. [23,24,53], for boost invariant systems.

C. Coulomb interaction

Particles that are nearby in phase space and carry the signal in the correlation function will also experience Coulomb interactions. This effect must be taken into account when extracting the HBT radii. Diferent methods of accounting for the Coulomb interaction were studied systematically in Ref. [33]. This analysis uses the Bowler-Sinyukov method [54,55]. The Coulomb interaction is computed for each pair with relative momentum components (q_o,q_s,q_l) that enters the analysis. The average interaction in each (q_o,q_s,q_l) bin is included as a constant, $K_{\rm Coul}$, in the fit parametrization. The quantity $K_{\rm Coul}$ is the squared Coulomb wave function integrated over the entire spherical Gaussian source. The same radius, 5 fm, is used as in earlier analyses. In Eq. (3), $K_{\rm Coul}$ only applies to the pairs nearby in phase space (the exponential term) and not to other particles accounted for by the $(1-\lambda)$ term.

In principle, correction for the Coulomb interaction between each particle and the mean field could also be taken into account. However, at the energies studied here, this interaction has been found to be negligible [56,57].

D. Event-plane calculations

The azimuthal analysis requires determining the event plane for each event, including applying appropriate methods to make the event-plane distribution uniform [58]. Uncertainty in the event plane reduces the extracted oscillation amplitudes of the HBT radii. The event plane resolutions must be computed to correct for this effect later in the analysis. The nth-order event-plane angle, ψ_n, is determined using charged particles measured in the TPC according to the equation

$$\psi_n = \frac{1}{n}\arctan\left(\frac{Q_y}{Q_x}\right) + \Delta\psi_n, \tag{4}$$

where the components of the event-plane vector are

$$Q_x = \frac{1}{N}\sum_i \left[w_i \cos(n\phi_i) - \langle Q\rangle_x\right], \tag{5}$$

$$Q_y = \frac{1}{N}\sum_i [w_i \sin(n\phi_i) - \langle Q\rangle_y]. \tag{6}$$

Here ϕ_i is the angle of the ith track and N is the total number of tracks used to determine the event plane. The shift correction [58] is given by

$$\Delta\psi_n = \sum_{\alpha=1}^{\alpha_{\rm max}} \frac{2}{\alpha}[-\langle\sin(n\alpha\psi_n)\rangle\cos(n\alpha\psi_n) + \langle\cos(n\alpha\psi_n)\rangle\sin(n\alpha\psi_n)], \tag{7}$$

where α determines the order $(n\alpha)$ that each correction term flattens. This analysis is performed relative to the second-order $(n=2)$ event plane.

For 7.7–39 GeV, the ϕ-weighting method [58–61] was used to flatten the event plane. The inverse, single-particle, azimuthal distribution is used to weight each particle in the event-plane determination so that inefficiencies do not affect the event-plane determination. The ϕ weight, $\phi_{{\rm wgt},i}$, is selected from this distribution for the ith particle using the direction of the particle's transverse momentum vector, $\vec{p}_{T,i}$. In this case $w_i = \phi_{{\rm wgt},i}\, p_{T,i}$ while the recentering terms $\langle Q\rangle_x$ and $\langle Q\rangle_y$, as well as the shift term $\Delta\psi_n$, are all zero.

For 62.4 and 200 GeV a problematic sector of the TPC was turned off causing a rather nonuniform azimuthal distribution. In this case the recentering and shift methods [58,60,62] were required to determine the event plane accurately. In this case, ϕ weights were not applied so $w_i = p_{T,i}$. Here the average offset in the direction of the p_T weighted flow vector, $\vec{Q}$, is used to compute $\langle Q\rangle_x$ and $\langle Q\rangle_y$. After this correction is applied, a shift method is needed to correct the event-plane values for effects owing to other harmonics. The shift term $\Delta\psi_n$ is determined by computing the correction terms $\langle\sin(n\alpha\psi_n)\rangle$ and $\langle\cos(n\alpha\psi_n)\rangle$ from $\alpha = 1$ up to $\alpha = 20$ terms, although generally $\alpha_{\rm max} = 2$ would be sufficient for a second-order analysis [58].

The event-plane resolution, $\langle\cos[2(\psi_{\rm EP} - \psi_2)]\rangle$, owing to differences between the reconstructed $(\psi_{\rm EP})$ and actual (ψ_2) reaction planes, is also needed as it enters the correction algorithm described later. The calculation begins by determining two event planes for two independent subevents which in this analysis correspond to the $\eta < 0$ and $\eta > 0$ regions, so-called η subevents. These subevent-plane estimates are processed through an iterative procedure to solve for the full event-plane resolution as outlined in Ref. [58]. Resolutions are reduced for lower multiplicity (and therefore lower energy) as well as more round (less anisotropic) cases. The values at each energy that enter this specific analysis are included in Fig. 3.

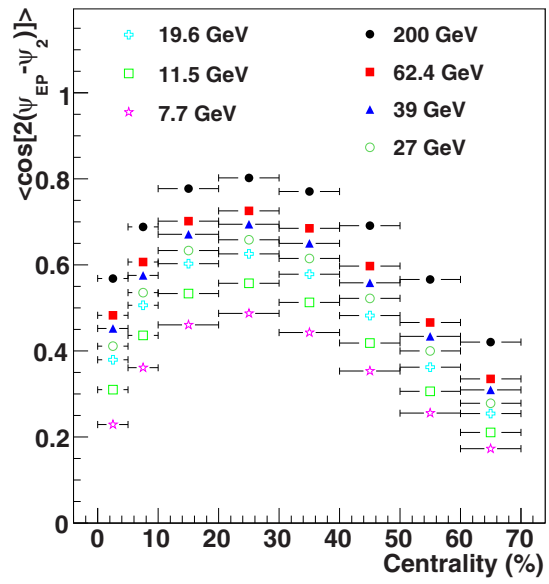

FIG. 3. (Color online) The event-plane resolutions for Au + Au collisions at $\sqrt{s_{NN}} = 7.7$, 11.5, 19.6, 27, 39, 62.4, and 200 GeV as a function of collision centrality. The resolutions, computed using the TPC $(|\eta| < 1)$, enter into both the correction algorithm and the global fit method. Statistical errors are smaller than the symbols.

TABLE II. The approximate systematic uncertainty on the HBT radii and freeze-out eccentricities.

Source	$R_{\rm out}$ (%)	$R_{\rm side}$ (%)	$R_{\rm long}$ (%)	$\varepsilon_{\rm F}$
Coulomb	4	3	4	0.004
Fit range	5	5	5	0.002
$F_{\rm MH}$	7	3	3	0.003
Total	9.5	6.5	7	0.005

E. Systematic uncertainties

The sources of systematic uncertainty have been studied in previous HBT analyses such as Refs. [33–35,40]. Similar studies have been used to estimate the systematic uncertainty owing to the Coulomb correction, fit range, and $F_{\rm MH}$ cut discussed earlier. The azimuthal analysis is most sensitive to the $F_{\rm MH}$ requirement and this is used to estimate the systematic uncertainty. For lower energies the dependence of the fit parameters on the allowed $F_{\rm MH}$ is consistent with earlier results at $\sqrt{s_{NN}} = 200$ GeV. Reduction of the Coulomb radius from 5 to 3 fm and variation of the fit range from 0.15 to 0.18 GeV/c also lead to results similar to those of earlier studies. Track splitting is effectively eliminated. The uncertainties are estimated to be the same for each $\sqrt{s_{NN}}$ reported here and are summarized in Table II, for each source, for the HBT radii and freeze-out eccentricity (defined in Sec. VI B 3).

Earlier STAR analyses [33–35,40] found, for various collision species ($p+p$, Cu + Cu, Au + Au) and data sets, that the systematic uncertainty is approximately 10% or less for the HBT radii in all centrality and k_T bins studied. Analogous studies lead to the same conclusion for the data sets used in the current analysis and suggest that the uncertainties are virtually independent of beam energy.

It should be noted that there is also an inherent uncertainty in the general method used to extract the eccentricity. The theoretical framework assumes a static, Gaussian region of homogeneity that corresponds to the entire volume of the collision at kinetic freeze-out. Flow-induced space-momentum correlations reduce this correspondence which could affect the reliability of the equations. However, several different model studies [23,24] find consistently that the results are still reliable to within 30%, even in the presence of strong flow. This would not affect any conclusions regarding the shape of the excitation function in regards to whether it is monotonic.

V. EXTRACTING RADIUS OSCILLATIONS

In azimuthally differential analyses, correlation functions are constructed for pairs directed at different angles relative to the event plane. The HBT radii that describe these regions exhibit sinusoidal variations relative to the event-plane direction. Second-order oscillations of these radii can be described in terms of Fourier coefficients which have been related to the eccentricity of the collision fireball at kinetic freeze-out. Owing to finite-bin-width and event-plane resolution, the amplitude of these oscillations is reduced from the actual value. To determine the true amplitudes, these effects must be taken into account. Three methods of correcting for these effects are described later in this section.

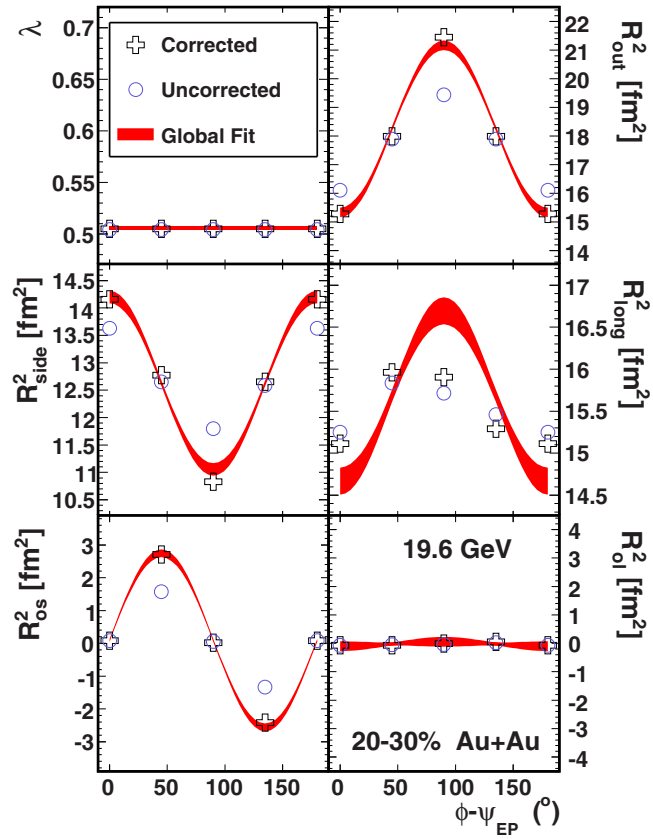

FIG. 4. (Color online) Examples of the angular oscillations of the HBT radii relative to the event plane from 20%–30% central, 19.6-GeV Au + Au collisions for $0.15 < k_T < 0.6$ GeV/c. Open circles show the radii before correction for finite-bin-width and event-plane resolution. Open cross symbols demonstrate that correcting these effects increases the oscillation amplitude. The corrected and uncorrected results are obtained with the HHLW fit method (see text) before and after the correction algorithm (Sec. V B) is applied. The points at 0° are repeated on the plot at 180° for clarity. The solid bands show the Fourier decomposition directly extracted using a global fit (Sec. V C) to all four angular bins; the width of the bands represent 1σ uncertainties from the fit. The value of λ is consistent for the two methods.

In the azimuthal HBT analysis, four correlation functions are constructed, for pairs directed in four different angular bins centered at $\Phi = 0°$, 45°, 90°, and 135° relative to the event plane. This allows extraction of the second-order sinusoidal variations of the HBT radii. Figure 4 shows an example of these oscillations. The Φ dependence of the HBT radii for a given beam energy, centrality, and k_T is described by

$$R^2_\mu(\Phi) = R^2_{\mu,0} + 2\sum_{n=2,4,6\ldots} R^2_{\mu,n}\cos(n\Phi) \quad (\mu{=}\mathrm{o,\ s,\ l,\ ol}) \qquad (8)$$

and

$$R^2_\mu(\Phi) = R^2_{\mu,0} + 2\sum_{n=2,4,6\ldots} R^2_{\mu,n}\sin(n\Phi) \quad (\mu = \mathrm{os}), \qquad (9)$$

where $R^2_{\mu,n}$ are the nth-order Fourier coefficients for radius term μ. These coefficients are computed using

$$R^2_{\mu,n} = \begin{cases} \langle R^2_\mu(\Phi)\cos(n\Phi)\rangle & (\mu = \text{o, s, l, ol}), \\ \langle R^2_\mu(\Phi)\sin(n\Phi)\rangle & (\mu = \text{os}). \end{cases} \quad (10)$$

The zeroth-order Fourier coefficients are expected to be nearly identical to radii extracted in an azimuthally integrated analysis. The second-order terms correspond to half the amplitude of the second-order oscillations for a second order, $n = 2$, analysis.

The extracted HBT radii display the expected [53] symmetries expressed in Eqs (10). The 3σ difference between the R^2_{long} values at 45° and 135° is eye catching, but is statistical in nature.

Imperfect event-plane resolution smears the difference between neighboring azimuthal bins and it also causes the peaks of the extracted oscillations of the HBT radii to appear smaller than they ideally should be. These effects must be corrected for to extract the true second-order oscillation amplitudes needed to compute the kinetic freeze-out eccentricities, ε_{F}, which are discussed in Sec. VI B 3. In the following discussion, two methods that have been applied in earlier analyses (which we refer to as the E895 and HHLW methods) are reviewed. A third method used in this analysis, dubbed the global fit method, is then introduced.

A. E895 method

In an earlier azimuthal HBT analysis performed by the E895 Collaboration [39] and a later analysis by the CERES Collaboration [42], the radii were extracted from correlation functions that were uncorrected for finite-bin-width and resolution effects. These uncorrected radii were then used to compute the Fourier coefficients described above. The uncorrected, second-order Fourier coefficients were then scaled by dividing by the event-plane resolution, as is done when correcting a v_2 measurement for event-plane resolution effects. While this is found to give consistent results to other methods described below, it is formally incorrect because it is not the radii that are smeared, but rather each q-space bin for each of the numerator, denominator, and Coulomb weighted mixed-event distributions separately. This method is referred to as the E895 method.

B. HHLW method

In this method, used first in Ref. [40], a model-independent correction algorithm is applied to compute the corrected numerator, denominator, and Coulomb weighted denominator histograms for each angular bin. The radii extracted from these corrected distributions are then used to compute the Fourier coefficients. This method is referred to as the HHLW method after the authors of the paper in which it was developed [53]. We briefly summarize this correction procedure below.

The derivation, detailed in Ref. [53], requires first decomposing mathematical expressions for the true (corrected) and experimental distributions as Fourier series. The true distributions are then convolved with a (Gaussian) distribution of the reconstructed event plane centered about the reaction plane and a function to account for the finite azimuthal bin width. Finally, each coefficient from the series for the true distribution is equated with the corresponding coefficient from the series expansion of the experimental distribution. This leads to the following relationship between coefficients for the true and experimentally observed distributions:

$$A^{\text{exp}}_{\alpha,n}(\vec{q}) = A_{\alpha,n}(\vec{q})\,\frac{\sin(n\Delta/2)}{n\Delta/2}\langle\cos[n(\psi_{\text{EP}} - \psi_2)]\rangle. \quad (11)$$

The quantities $A_{\alpha,n}(\vec{q})$ and $A^{\text{exp}}_{\alpha,n}(\vec{q})$ are the coefficients for the Fourier series representation of the true and experimental distributions, respectively. The formula applies separately to the numerator ($A = N$) and the denominator ($A = D$) of Eq. (2) and the Coulomb weighted mixed-event ($A = K_{\text{Coul}}$) distributions. The factors multiplying $A_{\alpha,n}(\vec{q})$ come from the convolution of the true series mentioned previously. The quantities $\langle\cos[n(\psi_{\text{EP}} - \psi_2)]\rangle$ are the reaction-plane resolutions. The symbol Δ is the width of each angular bin and n is the order of the Fourier coefficient. The experimental coefficients can be computed from the experimentally measured distributions in each angular bin using the standard definition for Fourier coefficients so that

$$A^{\text{exp}}_{\alpha,n}(\vec{q}) = \begin{cases} \langle A^{\text{exp}}_n(\vec{q},\Phi)\cos n\Phi\rangle & (\alpha = c) \\ \langle A^{\text{exp}}_n(\vec{q},\Phi)\sin n\Phi\rangle & (\alpha = s) \end{cases} \quad (12)$$

are the coefficients for the cosine ($\alpha = c$) or sine ($\alpha = s$) terms in the series expansion.

The corrected distributions can be computed from the experimental distributions using

$$A(\vec{q},\Phi_j) = A^{\text{exp}}(\vec{q},\Phi_j) + 2\sum_{n=1}^{n_{\text{bins}}}\zeta_n(\Delta) \times \left[A^{\text{exp}}_{c,n}(\vec{q})\cos(n\Phi_j) + A^{\text{exp}}_{s,n}(\vec{q})\sin(n\Phi_j)\right]. \quad (13)$$

In this analysis, only the second-order event plane, ψ_2, is measured, and so only the $n = 2$ terms are required. The correction parameter $\zeta_n(\Delta)$ is given by

$$\zeta_n(\Delta) = \frac{n\Delta/2}{\sin(n\Delta/2)\langle\cos[n(\psi_{\text{EP}} - \psi_2)]\rangle} - 1. \quad (14)$$

Substituting Eq. (14) into Eq. (13) leads to an identity, with only experimentally measured quantities on the right-hand side.

Once the corrected numerator, denominator, and Coulomb weighted mixed-event distributions are computed for each angular bin, fits are performed to extract the radii. As in Ref. [40], the λ parameter from the four angular bins are averaged (for each centrality) and set as a constant for all four bins; the $\langle\lambda\rangle$ values are nearly identical to the nonazimuthal cases. The correlation functions are refit to extract the radii. The λ-fixing procedure reduces the number of independent fit parameters needed. We have checked that removing this restriction from the fits results in no significant Φ dependence of λ, but only results in slightly larger errors for the radii, owing to the increase of parameters.

In any case, the HBT radii extracted from these corrected distributions exhibit the true, larger oscillation amplitude. This is clearly demonstrated in Fig. 4. One deficiency in this approach is that the uncertainties on the corrected distributions

are correlated, leading to an underestimate of the uncertainties for the extracted radii. We have developed a global fit method, described next, to avoid this issue.

C. Global fit method

A new global method of fitting was developed that avoids correlated errors and provides more reliable results in cases of low statistics and poor event-plane resolution. The method begins with the same Gaussian parametrization as in Eq. (3). The Fourier representation of the radii from Eqs. (8) and (9) are substituted, keeping only the zeroth- and second-order terms. In this method, the fit parameters are the Fourier coefficients that describe the oscillations of the radii relative to the event plane, and so the Fourier coefficients are extracted directly rather than the radii. Using this parametrization, the theoretical estimate of the true numerator, N^{true}, is then smeared for event-plane resolution and finite-binning effects by applying the correction algorithm in reverse, as described below. In this way, a theoretical estimate of the values expected in each uncorrected numerator, N^{smeared}, is obtained, which can then be compared to the uncorrected numerators that are experimentally measured, N^{exp}.

For each bin $\vec{q} = (q_{\text{o}}, q_{\text{s}}, q_{\text{l}})$, a value of the correlation function, $C^{\text{true}}(\vec{q})$, is computed. An estimate for the denominator is obtained from the "true" denominator, $D(\vec{q})$ (i.e., the denominator for a given Φ bin run through the correction algorithm described in the last section). The estimate for the true numerator, for each $\vec{q}$ bin, is simply $N^{\text{true}}(\vec{q}) = D(\vec{q})C^{\text{true}}(\vec{q})$. This value is then run through the correction algorithm in reverse. A series similar to Eq. (13),

$$N^{\text{smeared}}(\vec{q}, \Phi_j) = N^{\text{true}}(\vec{q}, \Phi_j) + 2\sum_{n=1}^{n_{\text{bins}}} \zeta_n'(\Delta) \times \left[N_{c,n}^{\text{true}}(\vec{q})\cos(n\Phi_j) + N_{s,n}^{\text{true}}(\vec{q})\sin(n\Phi_j)\right], \quad (15)$$

is used to compute the value expected to appear in the uncorrected numerator, N^{exp}, for each $(q_{\text{o}}, q_{\text{s}}, q_{\text{l}})$ bin and each Φ bin. The quantity N^{smeared} is the value expected in the uncorrected numerator, N^{exp}, based on the value, N^{true}, predicted by the current values of the fit parameters during each iteration of the fit algorithm. All fit parameters (including normalizations) obtained in this method correspond to the true correlation function even though the fit is applied to the uncorrected numerators. As in Eq. (13), only $n = 2$ terms are used for an analysis relative to the second-order event plane.

A factor similar to Eq. (14), from the same relationship between true and experimental values,

$$\zeta_n'(\Delta) = \frac{\sin(n\Delta/2)\langle\cos[n(\psi_{\text{EP}} - \psi_2)]\rangle}{n\Delta/2} - 1, \quad (16)$$

smears the true amplitude according to the resolution and finite-bin-width when substituted into Eq. (15).

In this way, an estimate, N^{smeared}, of the value that should be found in the uncorrected, raw numerator histogram, N^{exp}, for each $(q_{\text{o}}, q_{\text{s}}, q_{\text{l}})$ bin in each Φ bin is obtained from the fit function. The value expected by the fit function is compared to the value actually observed in each $(q_{\text{o}}, q_{\text{s}}, q_{\text{l}})$ bin in the four uncorrected numerator histograms for all four Φ bins in a single simultaneous "global" fit.

A separate normalization is used for each Φ bin because there will be differences in the number of tracks, and therefore pairs, in the different bins. A single λ parameter is used for all four angular bins, as is done in the HHLW fit method. The global fit method significantly reduces the number of parameters needed to describe the data from 21 parameters ($\lambda + 5$ radii $\times$ 4Φ bins) in the HHLW method to 11 parameters ($\lambda + 10$ Fourier coefficients), not counting the four normalization parameters.

The HHLW correction algorithm computes a corrected histogram from all of the uncorrected histograms. Therefore, the uncertainties in each corrected histogram depend on the uncertainties in all the uncorrected histograms. While the uncertainties are independent in the uncorrected histograms, the uncertainties in the "corrected" histograms are not. However, the fit assumes that the uncertainties are independent and, as a result, underestimates the true uncertainty. The new method, by fitting directly to the uncorrected numerator histograms, avoids this problem.

A disadvantage of the new algorithm is that the normalizations obtained correspond to the "true" correlation function, $C^{\text{true}}(\vec{q}) = N^{\text{true}}(\vec{q})/D^{\text{true}}(\vec{q})$, but the fit uses the corrected denominator histogram, $D(\vec{q})$, as in the HHLW method, and the uncorrected numerator histogram, $N^{\text{exp}}(\vec{q})$. To compare the fit to the distributions that are actually used in the fit, $C'(\vec{q}) = N^{\text{exp}}(\vec{q})/D(\vec{q})$, is projected onto the out, side, and long axes, but the normalizations do not correspond exactly. They do put the projections on a common scale, however. The 0° and 90° projections are shifted away from unity at large $\vec{q}$. Examples of the projections using the global fit method are shown in Fig. 5 for the same centrality and energy as the fits using the HHLW fit method, also shown in Fig. 5 for comparison. As a check, if instead one projects $N(\vec{q})/D(\vec{q})$ and $N^{\text{fit}}(\vec{q})/D(\vec{q})$, where $N^{\text{fit}}(\vec{q})$ is the unsmeared fit numerator computed from the extracted Fourier coefficients (from the global fit method), the projections look essentially identical to the HHLW fit method projections for all four angular bins.

For most centralities and fit parameters, the results agree quite well. However, the amplitude describing the R_{long}^2 oscillation, $R_{\text{l},2}^2$, is larger when obtained using the new fit method. This is demonstrated most clearly in Fig. 4 by comparing the solid band for the oscillation extracted using the global fit method to the corrected radii using the HHLW method. The difference in $R_{\text{l},2}^2$ for the two parametrizations means that the second order oscillation that best fits the data from all angular bins simultaneously is not consistent with the Gaussian R_{long} values that best describe the regions of homogeneity in each angular bin separately. While Gaussian fits are useful for characterizing overall system scales, it has been shown [33] that the correlation function at these energies is least Gaussian in the longitudinal direction. Hence, 5%–10% discrepancies in R_{long}^2 from different Gaussian fits is perhaps unsurprising.

The difference may be exacerbated by a subtle interdependence of the fit parameters in the HHLW fit method that constrains the R_{long} values. Also, the new fit method has

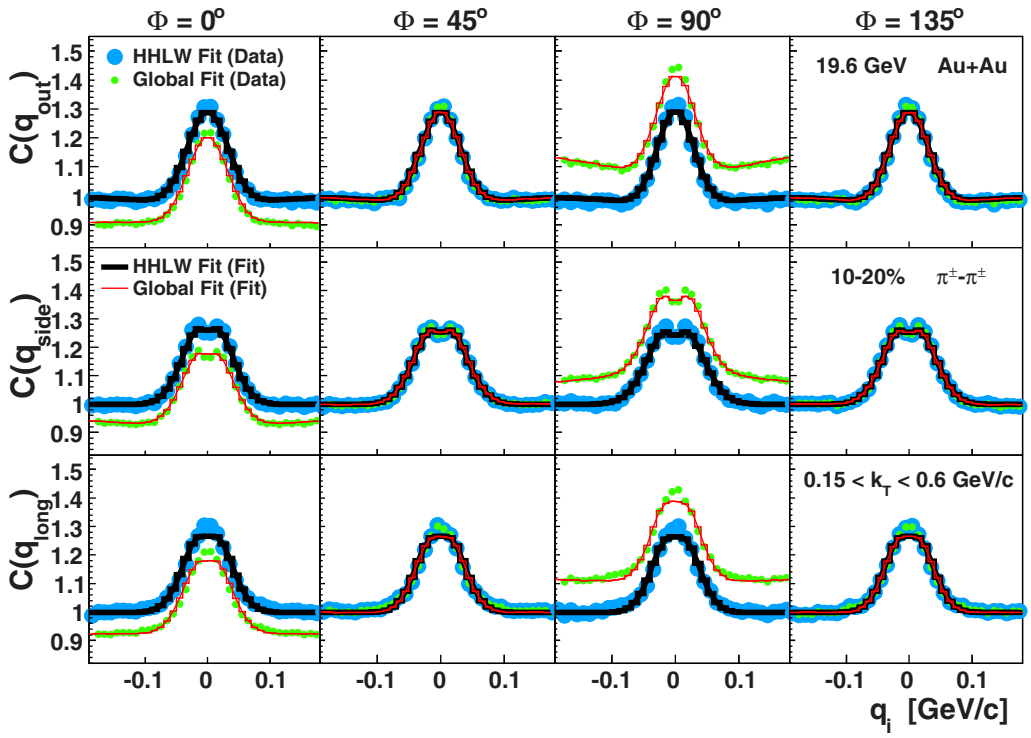

FIG. 5. (Color online) Sample fit projections onto the q_{out} (top row), q_{side} (middle row), and q_{long} (bottom row) axes for four angular bins relative to the reaction plane. Results from the HHLW fit method and the global fit method are shown for direct comparison. These projections are from results for 10%–20% central, 19.6-GeV Au + Au collisions with $0.15 < k_T < 0.6$ GeV/c.

difficulties in all central 0%–5% cases and in a few 5%–10% cases when the statistics become low. These cases are excluded, for instance, from Fig. 12, as well as all other figures for the azimuthally differential analysis. For some of the 0%–5% cases the fit could never converge even with high statistics. For these unreliable cases, while the $R^2_{\text{ol},2}$ values are close to zero in the HHLW fit results for all centralities, a large $R^2_{\text{ol},2}$ suddenly appears in this most central bin when using this global fit method. This is likely nonphysical because, for a symmetric acceptance window around midrapidity, R^2_{ol} must average to zero. Additionally, because the different angular bins are most similar in central events any second-order oscillation of $R^2_{\text{ol},2}$ should decrease in the most central bin owing to symmetry, not appear suddenly. In fact when $R^2_{\text{ol},2}$ is varied, the χ^2 value between the fit and the data becomes quite flat for the central data compared to other centralities allowing $R^2_{\text{ol},2}$ to take on a wide range of values without constraint. Additionally, when this happens the oscillations extracted for some, or sometimes all, of the other parameters ($R^2_{\text{o},2}$, $R^2_{\text{s},2}$, $R^2_{\text{l},2}$) change sign in this central case, even when statistics are high.

Owing to the symmetry of the almost round central events, the distributions for different angular bins are quite similar compared to other centralities. The global fit method extracts oscillations, not radii, from all four bins simultaneously, and when the distributions are similar it seems to have the freedom to find a wider variety of solutions. The HHLW fit method, with separate fits in each azimuthal bin, has no such freedom, but is found to be less reliable when statistics and resolutions are low. For the global fit method, for other centralities, the results are rather stable. The zeroth-order coefficients remain consistent with the azimuthally integrated results, which is even true for 0%–5% centrality. The behavior for central data appears to be the result of the relationship among the fit parameters used, the similar shape of the emission regions for all the angular bins in the central data, and the very shallow minimum in χ^2 that develops for $R^2_{\text{ol},2}$ at the same time. There are no other differences in the global fit algorithm compared to the HHLW fit method.

VI. RESULTS

The azimuthally integrated HBT results are discussed first and compared to historical data from earlier experiments and recent results from ALICE. Later, the azimuthally differential analysis is presented for a wide range of beam energies. The azimuthally differential analysis is also performed in three rapidity bins allowing extraction of the excitation function for the R^2_{ol} parameter and direct comparison of the freeze-out eccentricity in the same forward rapidity window as an earlier measurement by the CERES Collaboration. Finally, the excitation function for the freeze-out eccentricity is discussed along with its implications for the relevant underlying physics as outlined in Sec. II.

A. Azimuthally integrated HBT

There is a wealth of earlier HBT data demonstrating the systematic behavior of the HBT radii as a function of beam energy, k_T (or m_T), and centrality. Trends have been

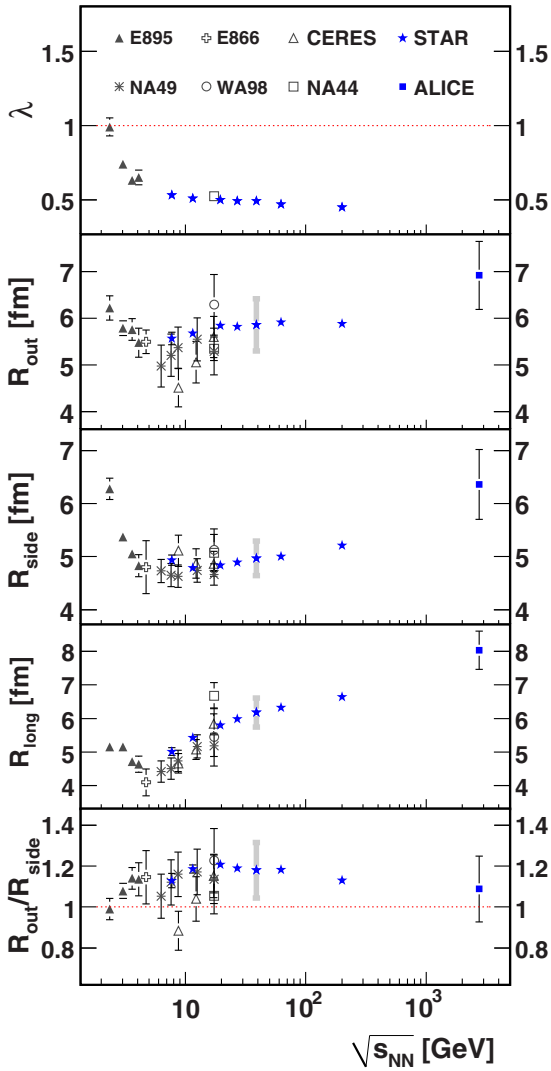

FIG. 6. (Color online) Energy dependence of the HBT parameters for central Au + Au, Pb + Pb, and Pb + Au collisions at midrapidity and $\langle k_T \rangle \approx 0.22$ GeV/c [26–31,36]. The text contains discussion about variations in centrality, k_T, and analysis techniques between experiments. Errors on NA44, NA49, WA98, CERES, and ALICE points include systematic errors. The systematic errors for STAR points at all energies (from Table II) are of similar size to the error bar for 39 GeV, shown as a representative example. Errors on other results are statistical only, to emphasize the trend. For some experiments the λ value was not specified.

established despite the measurements having been performed by various experiments and with differences in the analysis techniques. In this paper, the results are presented across a wide range of beam energies, overlapping previously measured regions and filling in previously unmeasured regions of $\sqrt{s_{NN}}$.

Figure 6 shows the beam energy dependence of the λ parameter, the HBT radii, and the ratio $R_{\rm out}/R_{\rm side}$ for like-sign pions in central collisions at low k_T. All the STAR results are from the most central 0%–5% and lowest $\langle k_T \rangle$ (≈0.22 GeV/c) data. The ALICE point is also from 0%–5% central data, but has a slightly larger $\langle k_T \rangle \approx 0.26$ GeV/c. Results from earlier experiments come from a range of central data sets, as narrow as 0%–7.2% to as wide as 0%–18% centrality, as well as a range of $\langle k_T \rangle$ values, from 0.17 to 0.25 GeV/c. The earlier data are from π^--π^- correlation results in which various methods of accounting for the Coulomb interaction were employed. The new STAR results are from combined π^--π^- and π^+-π^+ correlation functions. No significant difference between the two cases has been observed so the combination simply leads to higher statistics. Our high-statistics analysis, with identical acceptance for all $\sqrt{s_{NN}}$, yields a well-defined smooth excitation function consistent with the previous trends.

The λ parameter primarily represents the fraction of correlated pairs entering the analysis, as described in Sec. IV B. It decreases with increasing $\sqrt{s_{NN}}$ relatively rapidly at lower, AGS, energies while changing rather little from 7.7 to 200 GeV. This suggests that the fraction of pions in this $\langle k_T \rangle$ range from long-lived resonances increases at lower energy but remains rather constant at higher energies. The value of λ is larger than our earlier reported results for 200 GeV [33], which is related to our implementation of an antielectron cut that reduces contamination in this analysis. The $R_{\rm out}$ parameter similarly shows little change over a wide range of RHIC energies. It does appear to rise noticeably at the LHC. The values of $R_{\rm side}$ show a very small increase at the higher RHIC energies and a more significant increase at the LHC. The values of $R_{\rm long}$, however, appear to reach a minimum around 5 GeV, rising significantly at RHIC, and the ALICE point is once again higher than the trend observed at STAR.

The radius $R_{\rm side}$ is primarily associated with the spatial extent of the particle-emitting region, whereas $R_{\rm out}$ is also affected by dynamics [23,24] and is believed to be related to the duration of particle emission [63,64].

It has long been suggested [50,51,63] that a long particle-emission duration could result in $R_{\rm out}$ becoming much larger than $R_{\rm side}$. In the simplest scenario of a static, nonflowing source, the emission time is given by [65]

$$(\beta \Delta \tau_{\rm static}) = R^2_{\rm out} - R^2_{\rm side}, \tag{17}$$

where $\beta = \frac{k_T}{m_T}$ is the speed of one of the pions in the source rest frame. For a flowing source such as those created at RHIC, however, Eq. (17) is unreliable [22] as the dimensions of the homogeneity region probed by low-q pion pairs is affected differently in the out and side directions. Indeed, for some sources $R_{\rm out}$ may be smaller than $R_{\rm side}$ [23], in which case Eq. (17) would yield imaginary emission times.

It is interesting to note that the excitation function of this quantity shows a clear peak at $\sqrt{s_{NN}} \approx 20$ GeV, as seen in the top panel of Fig. 7. Clearly, Eq. (17) cannot be used, because $R^2_{\rm out} - R^2_{\rm side}$ becomes smaller as β increases and even becomes negative at higher $\sqrt{s_{NN}}$ and m_T. Extracting time scales from the quantity $R^2_{\rm out} - R^2_{\rm side}$ is necessarily model dependent.

Prompted by Rischke and Gyulassy [63], the ratio $R_{\rm out}/R_{\rm side}$ is frequently studied [22]. This ratio has the advantage of removing the overall scale of the system. Because $R_{\rm out}$ and $R_{\rm side}$ are both reduced by flow [23,66], their ratio is slightly more robust against flow effects. The ratio is also somewhat more natural to calculate in ideal (zero viscosity) hydrodynamic theory which has no intrinsic scale. Finally, extracting radii from dynamical model calculations depends

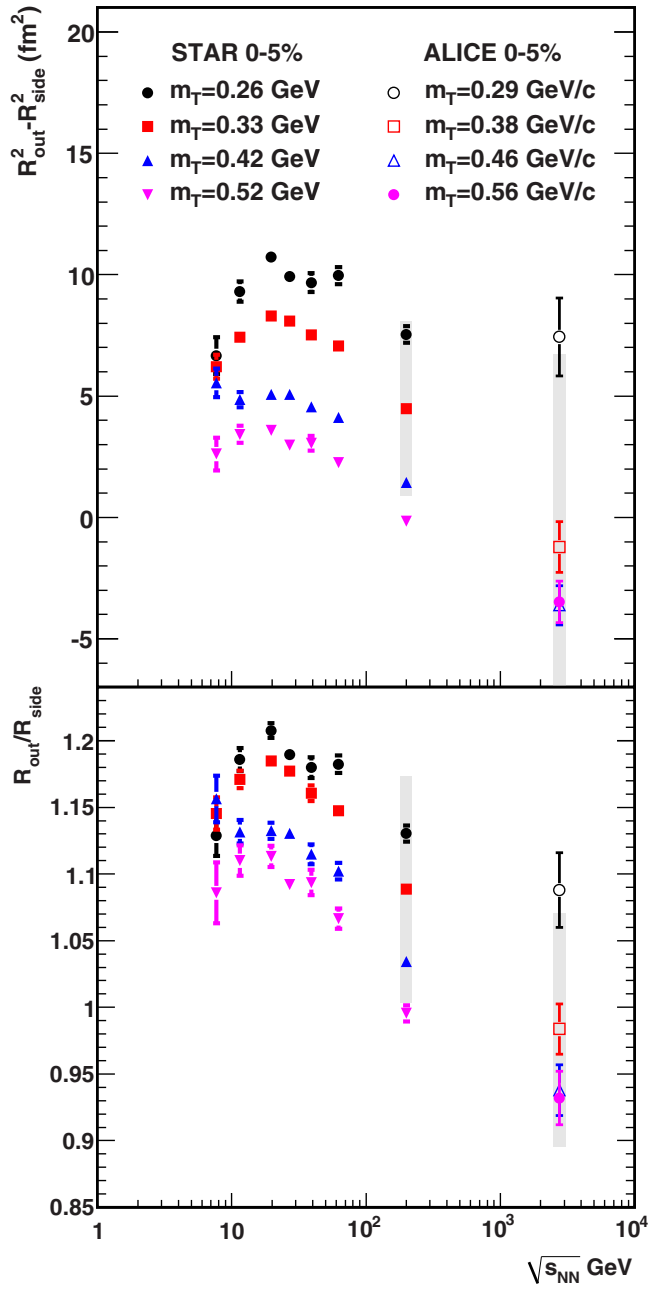

FIG. 7. (Color online) (Top) The difference between the squared transverse HBT radii are plotted as a function of the collision energy for STAR and ALICE measurements of the most central heavy ion collisions. (Bottom) The ratio of the out and side HBT radii for STAR and ALICE are plotted for the same collisions. In both cases, statistical errors are shown by solid error bars. Systematic errors are shown only for the data at $m_T = 0.33$ GeV ($m_T = 0.38$ GeV) for STAR (ALICE); systematic errors are common for all m_T cuts. The systematic errors are driven by two-track cuts that are common to all STAR energies and so are drawn only for the $\sqrt{s_{NN}} = 62.4$-GeV data.

on the algorithm used [22]. Calculations that rely strictly on freeze-out distributions and bypass calculation of the momentum-space correlation function, often yield HBT radii that are much too large, whereas the ratios between them are closer to experimental values [22,67].

In the hydrodynamic calculation of Rischke and Gyulassy, which included flow, $R_{\rm out}/R_{\rm side}$ exhibited a peak as the energy density of the system nears the threshold of a first-order phase transition or rapid crossover transition [63]. This ratio is shown in the bottom panel of Fig. 6 for the world's data set. A small peaking behavior in the STAR data is obscured by the historical SPS and AGS data. The excitation function is clearer if the STAR and ALICE data are viewed separately, as seen in the bottom panel of Fig. 7 [68]. For all m_T ranges, the ratio peaks at $\sqrt{s_{NN}} \approx 20$ GeV.

It is not unreasonable to examine the RHIC and LHC data on their own. Femtoscopic techniques, including various methods for accounting for the Coulomb repulsion between the pions, have evolved over time [22]; STAR and ALICE use the Bowler-Sinyukov formalism [54,55], which affects particularly the outward radius [33]. Furthermore, the detector acceptance and two-track efficiency change as a function of collision energy in a fixed-target experiment, which can complicate detection of a subtle trend in an observable with $\sqrt{s_{NN}}$. Midrapidity measurement with collider experiments such as STAR and ALICE are performed with uniform coverage independent of collision energy. Finally, systematic errors vary from one experiment to another. While the systematic error on $R_{\rm out}/R_{\rm side}$ (shown as a gray band in Fig. 7) is significant, it is common for all $\sqrt{s_{NN}}$, so the peak in the ratio is statistically significant.

The peak in $R^2_{\rm out} - R^2_{\rm side}$ and $R_{\rm out}/R_{\rm side}$ is intriguing, especially because it occurs around a collision energy where several other observables [69–72] show nontrivial trends that may indicate a change in the underlying physics at these energies. However, conclusive interpretation of the femtoscopic data presented here must await comparison with theoretical calculations.

The value of $R_{\rm long}$ has been related to the kinetic freeze-out temperature, T, and lifetime, τ, of the system by the relation [23,73,74]

$$R_{\rm long} = \tau \sqrt{\frac{T}{m_T} \frac{K_2(m_T/T)}{K_1(m_T/T)}}, \tag{18}$$

where $K_1(m_T/T)$ and $K_2(m_T/T)$ are modified Bessel functions. The kinetic freeze-out temperature is not expected to change much with $\sqrt{s_{NN}}$. Therefore, the rise of $R_{\rm long}$ suggests that the total lifetime of the system is increasing with energy. At the end of this section Eq. (18) is used to extract τ as a function of $\sqrt{s_{NN}}$ given certain assumptions.

The systematic errors for STAR points at all energies (from Table II) are of similar size to error bar for 39 GeV, shown as a representative example. Errors on other results are statistical only to emphasize the trend.

Figure 8 shows the $\langle m_T \rangle$ dependence of the HBT parameters for each energy. As mentioned earlier, the decrease in transverse and longitudinal radii at higher m_T are attributed to transverse and longitudinal flow [23,66]. Larger m_T pairs are emitted from smaller emission regions with less correspondence to the size of the entire fireball. For both $R_{\rm out}$ and $R_{\rm side}$ the different beam energies show similar trends in both magnitude and slope. For $R_{\rm long}$, the slopes appear to remain similar for the different energies, but the magnitude of $R_{\rm long}$ increases with energy for all centralities. From these observations, and

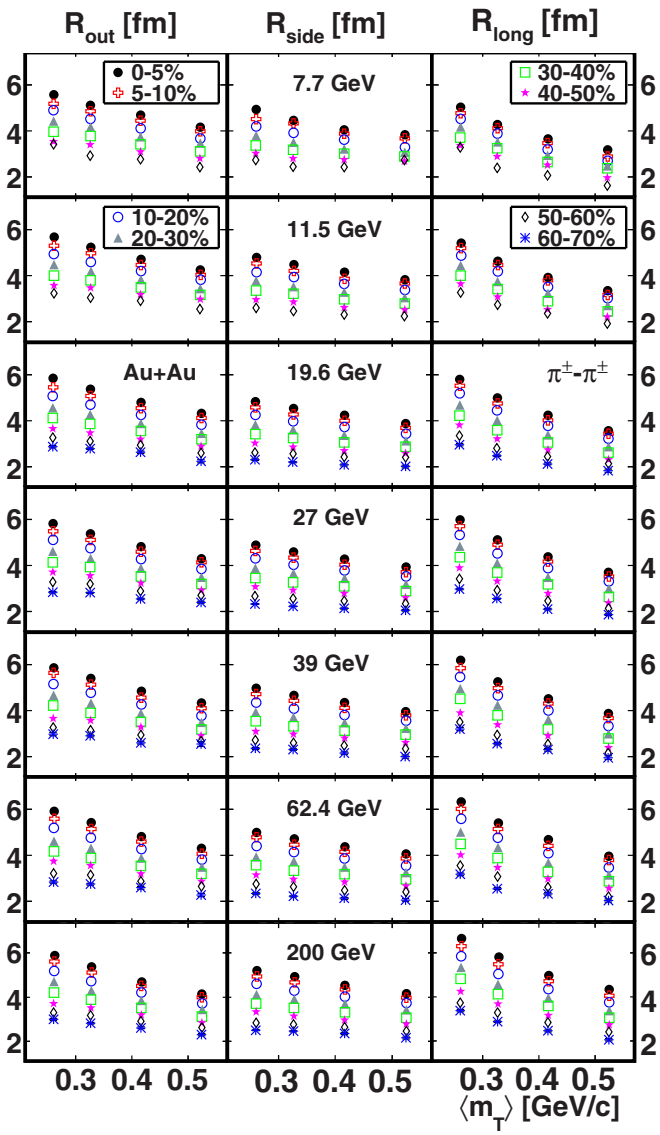

FIG. 8. (Color online) The $\langle m_T \rangle$ dependence of $R_{\rm out}$, $R_{\rm side}$, and $R_{\rm long}$ for each energy and multiple centralities. Errors are statistical only. For 7.7 and 11.5 GeV, the results for 60%–70% centrality are excluded owing to lack of statistics.

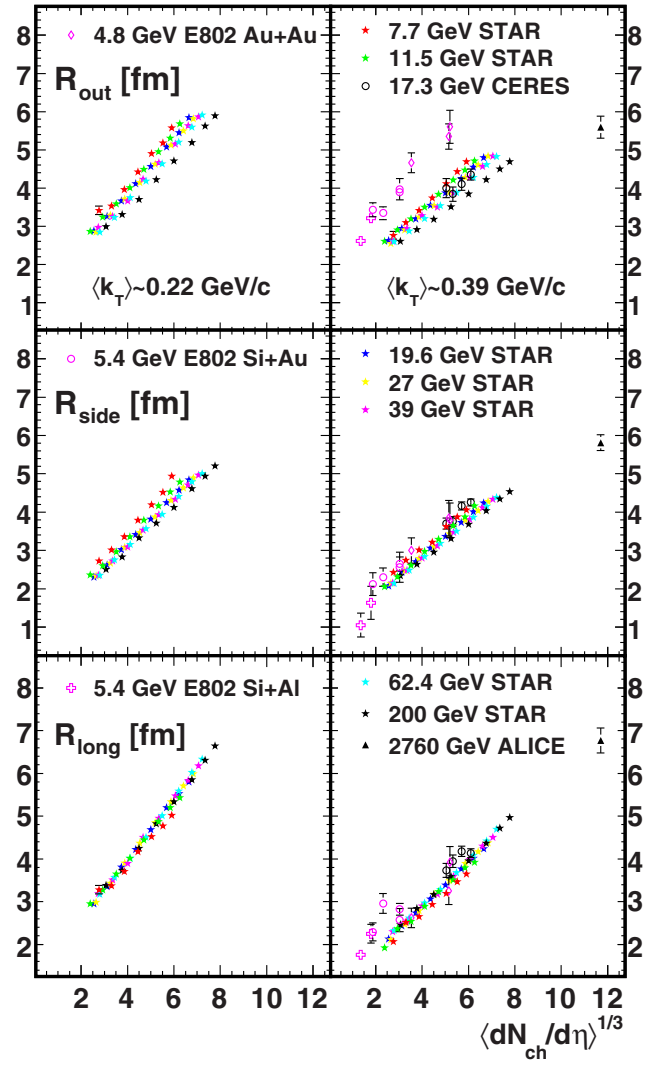

FIG. 9. (Color online) The dependence of the HBT radii on multiplicity, $\langle dN_{\rm ch}/d\eta \rangle^{1/3}$, for $\langle k_T \rangle \approx 0.22$ GeV/c (left) and $\langle k_T \rangle \approx 0.39$ GeV/c (right). Results are for Au + Au collisions at STAR, Pb + Au at CERES [28], Pb + Pb at ALICE [36], and Si + A at E802 [25]. Errors are statistical only.

considering that Fig. 6 showed the beam energy dependence for a single k_T and centrality bin, it is apparent that similar dependencies on $\sqrt{s_{NN}}$ exist for all the studied centrality and k_T ranges.

The multiplicity dependencies of the HBT radii are presented in Fig. 9 for two k_T ranges with $\langle k_T \rangle \approx 0.22$ GeV/c and $\langle k_T \rangle \approx 0.39$ GeV/c. A few earlier measurements with similar $\langle k_T \rangle$ are shown as well. It was observed in Ref. [34] that both $R_{\rm side}$ and $R_{\rm long}$ follow a common universal trend at 62.4 and 200 GeV independent of the collision species. ALICE has recently shown that $p + p$ collisions exhibit a different multiplicity dependence with a smaller slope [37,38]. The difference may be attributable to the interactions in the bulk medium formed in heavy ion collisions.

The results from ALICE are at different $\langle k_T \rangle$ values. To get a similar $\langle k_T \rangle \approx 0.39$ GeV/c estimate, the ALICE data points [36] reported for $\langle k_T \rangle \approx 0.35$ GeV/c and $\langle k_T \rangle \approx 0.44$ GeV/c are averaged and plotted in Fig. 9. There is some ambiguity in this approach as the different pair statistics at different k_T are not accounted for when averaging this way. As demonstrated in Refs. [36–38], the universal trends for $R_{\rm side}$ and $R_{\rm long}$ continue up to LHC energies.

When comparing different data sets from previous analyses [25,28,36], there is an uncertainty on the centrality caused by the different techniques that were used to compute the average charged track multiplicity $\langle dN_{\rm ch}/d\eta \rangle$. In this analysis, the standard STAR centrality definition was used at all energies, where $\langle dN_{\rm ch}/d\eta \rangle$ is computed using all events that pass the event selection cuts. However, it should be noted that this is an uncorrected value of $\langle dN_{\rm ch}/d\eta \rangle$ that underestimates the true value, thus allowing for a qualitative comparison only with other experiments.

An estimate of the volume of the homogeneity regions, $V = (2\pi)^{3/2} R_{\rm side}^2 R_{\rm long}$, can be computed using the data in

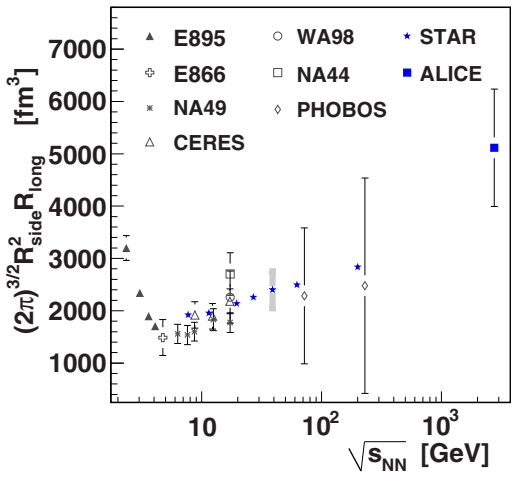

FIG. 10. (Color online) The beam energy dependence of the volume, $V = (2\pi)^{3/2} R^2_{\rm side} R_{\rm long}$, of the regions of homogeneity at kinetic freeze-out in central Au + Au, Pb + Pb, and Pb + Au collisions with $\langle k_T \rangle \approx 0.22$ GeV/c [26–32,36]. The systematic errors for STAR points at all energies (from Table II) are of similar size to the error bar for 39 GeV, shown as a representative example. Errors on other results are statistical only, to emphasize the trend. The PHOBOS points are offset in $\sqrt{s_{NN}}$ for clarity. The text contains some discussion about variations in centrality, $\langle k_T \rangle$, and analysis techniques between different experiments.

Fig. 6. These values are plotted in Fig. 10 as a function of $\sqrt{s_{NN}}$. The STAR results are all for 0%–5% central collisions with $\langle k_T \rangle \approx 0.22$ GeV/c. Because the values are computed using the data in Fig. 6, all the same variations in centrality ranges and $\langle k_T \rangle$ values are present in the volume estimates too. Earlier results from other experiments suggest a minimum between AGS and SPS energies. The STAR results show a noticeable increase in volume at the higher energies while the 7.7- and 11.5-GeV points are almost the same, consistent with a minimum in the vicinity of 7.7 GeV. The ALICE point rises even further, suggesting that the regions of homogeneity are significantly larger in collisions at the LHC.

The CERES Collaboration [75] has found that a constant mean free path at freeze-out,

$$\lambda_F \approx \frac{V}{(N_\pi \sigma_{\pi\pi} + N_N \sigma_{\pi N})} \approx 1 \text{ fm}, \tag{19}$$

leads naturally to a minimum in the energy dependence of the volume that is observed, assuming that the cross sections $\sigma_{\pi\pi}$ and $\sigma_{\pi N}$ depend weakly on energy, because the yields of pions and nucleons, N_π and N_N, change with energy. Above 19.6 GeV, the ratio of $N_\pi \sigma_{\pi\pi}/N_N \sigma_{\pi N}$ remains rather constant and the denominator in Eq. (19) increases with energy similar to the volume. Below 11.5 GeV, the $N_N \sigma_{\pi N}$ term becomes the dominant term and it increases at lower energies as does the volume. At higher energies, this scenario is consistent with the nearly universal trend of the volume on $\langle dN_{\rm ch}/d\eta \rangle$ and, therefore, $R_{\rm side}$ and $R_{\rm long}$ on $\langle dN_{\rm ch}/d\eta \rangle^{1/3}$ [34]. It is interesting that the multiplicity dependence for $R_{\rm side}$ begins to deviate slightly from this trend for 7.7 and 11.5 GeV in Fig. 9, which is the same region where the system changes from π-N to π-π dominant. Also, the argument above neglects the influence from less abundant species including kaons, but it has been observed that strangeness enhancement occurs in this same region of $\sqrt{s_{NN}}$ [76].

Another change that occurs in this region is the rapid increase of v_2 around $\sqrt{s_{NN}} = 2$–7 GeV. In the region around 7.7 to 11.5 GeV, the slope of $v_2(\sqrt{s_{NN}})$ begins to level off [49,77]. A possibility is that the deviation of $R_{\rm side}$ for 7.7 and 11.5 GeV is related to the onset of flow-induced space-momentum correlations. The E802 results at 4.8 and 5.4 GeV in the right column of Fig. 9 are qualitatively similar to the STAR 7.7 GeV results for $R_{\rm side}$, but considering that the STAR $\langle dN_{\rm ch}/d\eta \rangle^{1/3}$ values are slightly underestimated, the E802 results probably deviate slightly more relative to the higher energies than even the 7.7-GeV data. For $R_{\rm out}$, however, the E802 results are significantly larger than the STAR 7.7-GeV points. This could be consistent with the effects of flow. Transverse flow should reduce the size of the regions of homogeneity and is expected to affect $R_{\rm out}$ much more than $R_{\rm side}$. This was reflected already in the larger slope for the $\langle m_T \rangle$ dependence of $R_{\rm out}$ relative to $R_{\rm side}$ in Fig. 8. It would be interesting to study these trends at lower energies with a single detector where many interesting physical changes are occurring simultaneously.

An alternative explanation of the minimum observed in the volume measurement in Fig. 10 is provided by ultrarelativistic quantum molecular dynamics (UrQMD) calculations. In Ref. [78], UrQMD also finds a minimum between AGS and SPS energies but, in this case, the cause is related to a different type of change in the particle production mechanism. At the lowest energies pions are produced by resonances, but as the energy increases more pions are produced by color string fragmentation (accounting for color degrees of freedom) which freeze out at an earlier, smaller stage (thus, a smaller volume is measured). At even higher energies, the large increase in pion yields cause the volume to increase once more. This explanation suggests that a change from hadronic to partonic degrees of freedom cause the minimum in the volume measurement. Allowing a mean-field potential to act on these preformed hadrons (the color string fragments) leads UrQMD to predict $R_{\rm out}/R_{\rm side}$ values near the observed values ($\approx$1) for the whole energy range from AGS to SPS [79]. Simultaneously, inclusion of the mean field for preformed hadrons causes UrQMD to reproduce the net proton rapidity distribution and slightly improves its prediction for $v_2(p_T)$ at intermediate p_T.

As one last application of the data, the lifetime of the collisions is extracted in a study analogous to Ref. [36]. We also assume a kinetic freeze-out temperature of $T = 0.12$ GeV and fit the data in Fig. 8 using Eq. (18). The results are plotted in Fig. 11. The STAR results are all for 0%–5% collisions with $\langle k_T \rangle \approx 0.22$ GeV/c. Again, there are some variations in the centrality ranges, as in Fig. 6, for the historical data. The extracted lifetime appears to increase from around 4.5 fm/c at the lowest energies to around 7.5 fm/c at 200 GeV, an increase of an approximate factor of 1.7. The ALICE point suggests a much longer-lived system, above the trend observed at lower energies. Varying the temperature assumed in the fits to $T = 0.10$ GeV to $T = 0.14$ GeV causes the lifetimes to

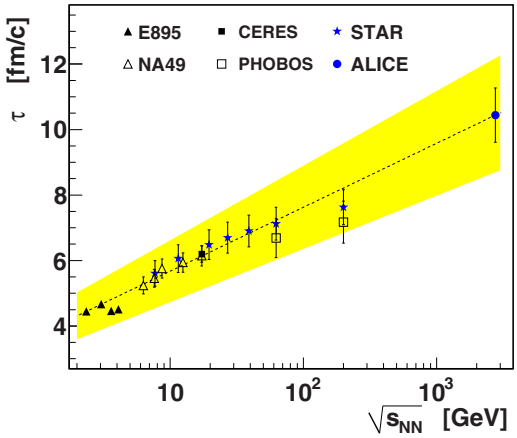

FIG. 11. (Color online) The lifetime, τ, of the system as a function of beam energy for central Au + Au collisions assuming a temperature of $T = 0.12$ GeV at kinetic freeze-out. Statistical uncertainties from the fits are smaller than the data points. For all experiments except E895, which did not report systematic uncertainties, error bars indicate systematic uncertainties, based on reported systematic uncertainty on $R_{\rm long}$. The line extrapolates between the lowest and highest energy. The text contains a discussion about variations in centrality and analysis techniques between different experiments. The yellow band demonstrates the effect on τ of varying the assumed temperature by ± 0.02 GeV.

increase by 13% and decrease by 10%, respectively, for all energies, as indicated by the yellow band. As noted in Ref. [36], owing to effects from nonzero transverse flow and chemical potential for pions, the use of Eq. (18) may significantly underestimate the actual lifetimes.

B. Azimuthally differential HBT

The detailed results of the azimuthally differential analysis are presented in Figs. 12 through 27. Earlier, Fig. 4 presented an example of the second-order oscillations of the HBT radii relative to the event plane for a single energy, centrality, and rapidity. These second-order oscillations are represented by zeroth- and second-order Fourier coefficients, as described in Sec. V A. The Fourier coefficients are presented as a function of $N_{\rm part}$ in two figures for each energy, starting with Figs. 12 and 13 for 7.7 GeV and continuing through Figs. 24 and 25 for 200 GeV. For each energy, the first figure compares midrapidity results from the HHLW and global fit methods while the second compares forward, backward, and midrapidity results obtained using the global fit method. Each set of Fourier coefficients for a given $N_{\rm part}$ (centrality), rapidity, and energy encodes all the information for oscillations similar to those in Fig. 4.

In each of the figures showing the Fourier coefficients, the zeroth-order coefficients are presented in the middle column, for the squared radii in the out, side, and long directions ($R^2_{\rm o,0}$, $R^2_{\rm s,0}$, $R^2_{\rm l,0}$) and the out-side cross term ($R^2_{\rm os,0}$). These values are expected to correspond to radii from the azimuthally integrated analysis. This correspondence is demonstrated in the first Fourier coefficient figure for each energy which also includes the azimuthally integrated results (red crosses) for direct comparison. As in the azimuthally integrated case,

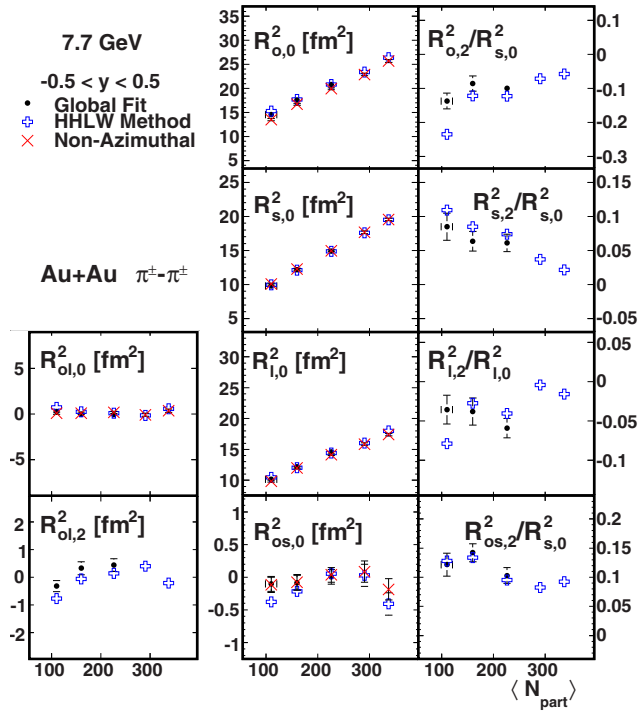

FIG. 12. (Color online) Centrality dependence of the Fourier coefficients that describe azimuthal oscillations of the HBT radii, at midrapidity ($-0.5 < y < 0.5$), in 7.7-GeV collisions with $\langle k_T \rangle \approx 0.31$ GeV/c. Open symbols are results using separate Gaussian fits to each angular bin, the HHLW method. Solid circles represent results using a single global fit to all angular bins to directly extract the Fourier coefficients. Crosses directly compare the azimuthally integrated radii and the zeroth-order Fourier coefficients. Error bars include only statistical uncertainties. The 0%–5% and 5%–10% global fit points have been excluded.

the diagonal radii increase with centrality, while the $R^2_{\rm os,0}$ cross term remains about zero for all centralities. In the right column of these figures, ratios of second-order to zeroth-order coefficients are presented, also for the out, side, long, and out-side parameters. The ratios that are presented have been connected to the freeze-out geometry, especially for the $R^2_{\rm s,2}/R^2_{\rm s,0}$ case. The left column of each of the figures contains the parameters for the out-long cross term. The zeroth-order values, $R^2_{\rm ol,0}$, are nonzero away from midrapidity and show interesting dependence on energy and centrality that is discussed later.

1. *Comparison of fit methods*

This section provides a comparison of the HHLW fit method and the global fit method used in the azimuthally differential analysis at midrapidity. The first Fourier coefficient figure for each energy is relevant for this discussion. For Sec. VI B 2, the second Fourier coefficient figure for each energy is relevant for the discussion of centrality and rapidity dependence of the Fourier coefficients.

The results using the two fit methods are generally consistent for most of the parameters. For each energy, the first figure compares the Fourier coefficients from the two fit methods at

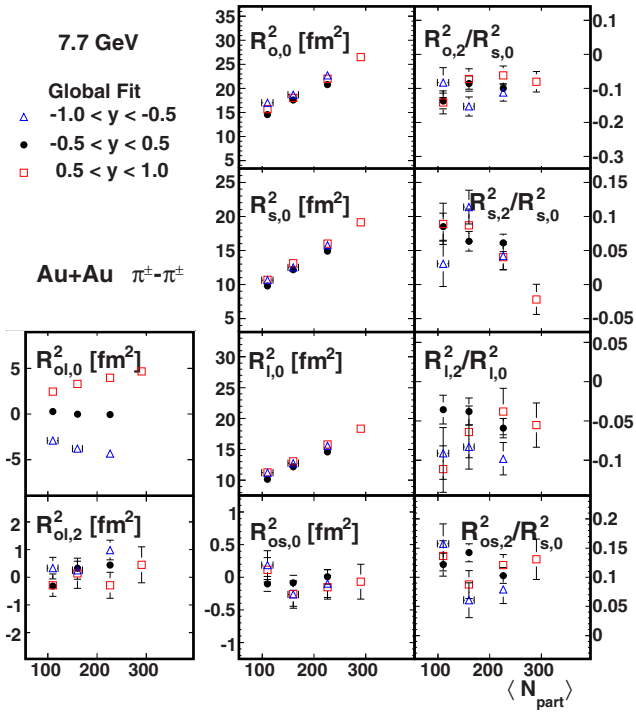

FIG. 13. (Color online) Centrality dependence of the Fourier coefficients that describe azimuthal oscillations of the HBT radii, at backward ($-1 < y < -0.5$), forward ($0.5 < y < 1$), and mid-($-0.5 < y < 0.5$) rapidity, in 7.7-GeV collisions with $\langle k_T \rangle \approx 0.31$ GeV/c using the global fit method. Error bars include only statistical uncertainties. The 0%–5% and two 5%–10% points have been excluded.

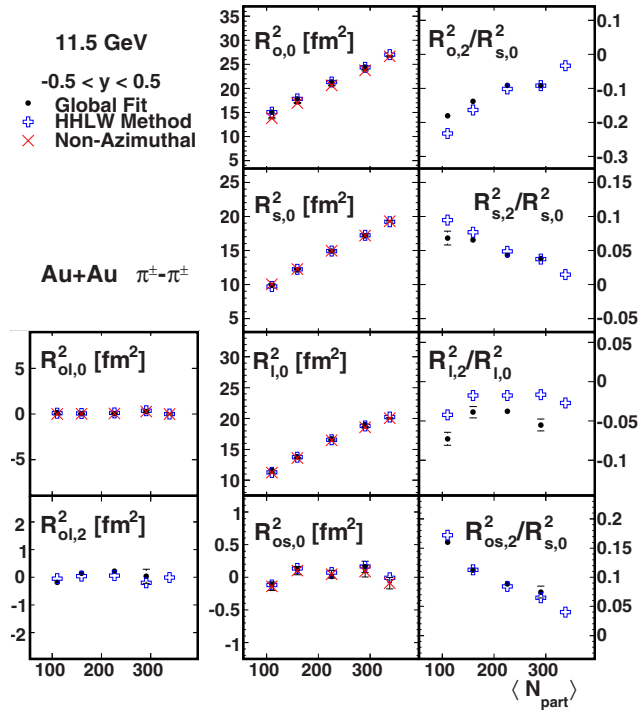

FIG. 14. (Color online) Centrality dependence of the Fourier coefficients that describe azimuthal oscillations of the HBT radii, at midrapidity ($-0.5 < y < 0.5$), in 11.5-GeV collisions with $\langle k_T \rangle \approx 0.31$ GeV/c. The symbols have the same meaning as in Fig. 12. Error bars include only statistical uncertainties. The 0%–5% global fit point is excluded.

midrapidity. Forward and backward rapidity results are not included as some of the results become unreliable in a few cases. The reason is that at the lowest energies statistics limits the reliability of the HHLW fit method, especially for 7.7 GeV, which has the fewest events and the lowest multiplicity per event. The forward and backward rapidity regions have even lower statistics owing to the narrower window of rapidity, $\Delta y = 0.5$ rather than $\Delta y = 1$. As seen in Fig. 3, the event-plane resolutions are much lower at these energies as well, which can amplify noise in the correlation function when the correction algorithm is applied. The correction algorithm does not distinguish between a real signal and a statistical variation. The amplitude of the variations is increased in either case. The global fit method was designed to minimize this problem by only applying the correction algorithm to the denominator which has an order of magnitude higher statistics than the numerator.

The zeroth-order Fourier coefficients are expected to be consistent with the radii in the azimuthally integrated analysis. Therefore, the zeroth-order, squared radii should increase smoothly with $N_{\rm part}$ (as in the middle column of Figs. 12 through 25). For the zeroth-order terms good agreement with the azimuthally integrated results is observed for both the HHLW and the global fit methods, except a few cases at the lowest energies. Especially for 7.7 GeV, with the HHLW fit method, several points, primarily the most peripheral and more central (lowest statistics and resolution) points, were found to deviate quite significantly from this trend. All of these points are excluded in the figures because they are unreliable. In the same cases, however, the global fit method remains consistent with the nonazimuthal radii. Projections of the fits on the out, side, and long axes show the HHLW fit method results do not match well with the data in such cases. In particular, the 90° bin suffers most from low statistics (fewer tracks are directed out of the reaction plane), which affects both the zeroth- and second-order coefficients when each bin is fit separately. The global fit method results are somewhat more reliable in these low-statistics and low-resolution cases.

As noted earlier, there is a difference in the oscillation amplitude for the long direction, $R^2_{\rm l,2}$, obtained from the two methods. This is shown clearly in Fig. 4 where the global fit method extracts a larger oscillation amplitude. From the first Fourier coefficient figure at each energy, the ratio $R^2_{\rm l,2}/R^2_{\rm l,0}$ is systematically further below zero for the global fit method results. This is a systematic difference, independent of centrality and energy, related to the different parametrizations in the two fit methods.

For reasons discussed in Sec. V C, results using the global fit method are not shown for the most central 0%–5% data, as well as a few 5%–10% cases for 7.7 and 11.5 GeV, where the statistics are low. Still, in all cases, the fit projections from the global fit method better match the data, there is better agreement between forward and backward as well as midrapidity results and, as discussed in Sec. V C, the errors are not underestimated as they are for the HHLW fit method.

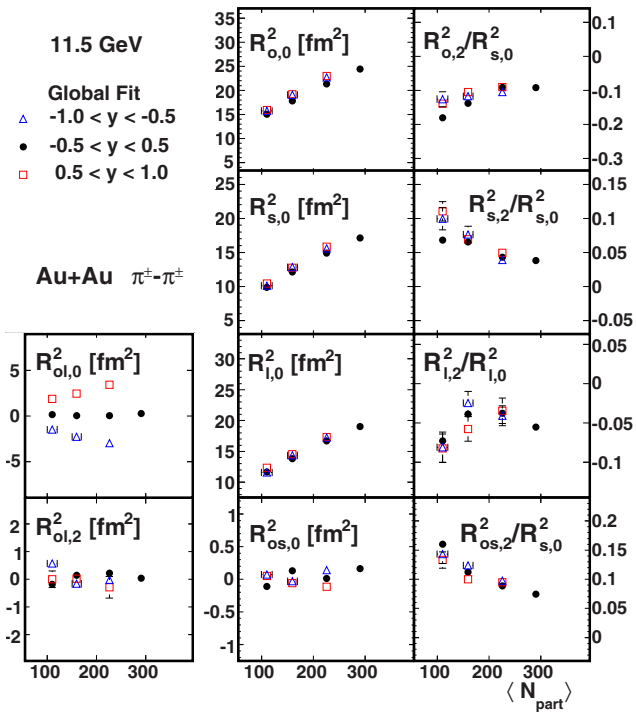

FIG. 15. (Color online) Centrality dependence of the Fourier coefficients that describe azimuthal oscillations of the HBT radii, at backward ($-1 < y < -0.5$), forward ($0.5 < y < 1$), and mid- ($-0.5 < y < 0.5$) rapidity, in 11.5-GeV collisions with $\langle k_T \rangle \approx 0.31$ GeV/c using the global fit method. Error bars include only statistical uncertainties. The 0%–5% and two 5%–10% points have been excluded.

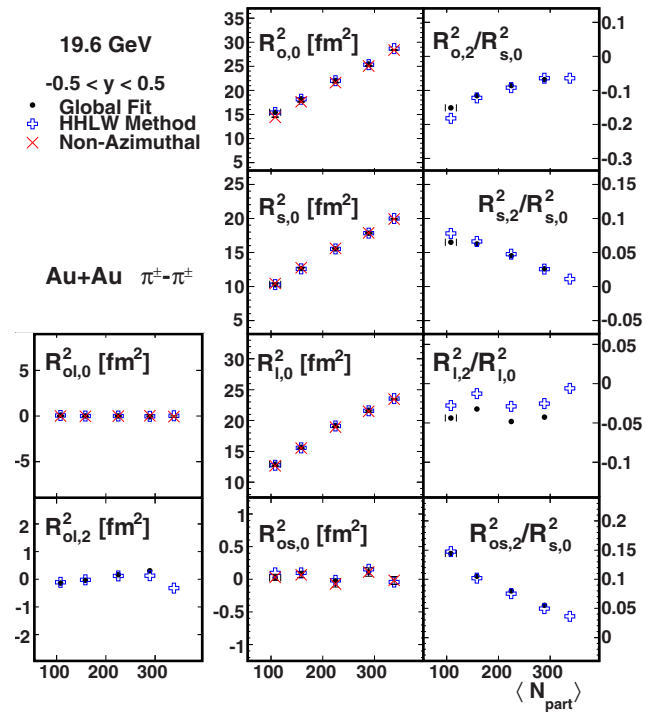

FIG. 16. (Color online) Centrality dependence of the Fourier coefficients that describe azimuthal oscillations of the HBT radii, at midrapidity ($-0.5 < y < 0.5$), in 19.6-GeV collisions with $\langle k_T \rangle \approx 0.31$ GeV/c. The symbols have the same meaning as in Fig. 12. Error bars include only statistical uncertainties. The 0%–5% global fit point is excluded.

Therefore, results using the global fit method are used later when discussing the freeze-out shape.

2. *Fourier components*

The trends exhibited by the Fourier coefficients are qualitatively similar for all energies. The zeroth-order coefficients are consistent with the nonazimuthal results. Like in the nonazimuthal results, the increase of the zeroth-order coefficients for more central data is related to the increasing volume of the homogeneity regions in more central events. Because the ratios of second- to zeroth-order results are related to the freeze-out shape, the trends are expected to extrapolate toward zero for more central, more round collisions. The right column of the Fourier coefficient figures for each energy demonstrate that this behavior is observed. For each HBT radius, the ratios of second- to zeroth-order coefficients follow similar trends for all energies, rapidities, and centralities. This means that the second-order coefficients (half the oscillation amplitudes) have the same sign in all these cases. Therefore, the data requires that all energies, rapidity ranges, and centralities must exhibit oscillations of the HBT radii that are qualitatively similar to those in Fig. 4. The Fourier coefficients for all three rapidities are similar in most cases, especially in the $R^2_{s,2}/R^2_{s,0}$ values for 10%–20% and 20%–30% centralities used later in the excitation function for the freeze-out eccentricity.

One interesting feature occurs in the $R^2_{ol,0}$ parameter at forward and backward rapidity. This parameter exhibits both centrality and energy dependence that may be relevant for constraining future model studies. The centrality dependence is shown in the top panel in the left column of Figs. 13, 15, 17, 19, 21, 23, and 25. As discussed earlier, this term averages to zero for results centered at midrapidity, but is otherwise nonzero. At the lowest energy, the $R^2_{ol,0}$ offset is quite large (Fig. 13) and increases in a linear manner with $N_{\rm part}$. At higher energies, although the linear trend with $N_{\rm part}$ remains, the slope decreases for larger $\sqrt{s_{NN}}$. For the 200-GeV results in Fig. 25, the slope and values are quite small compared to the 7.7-GeV case, for instance. As discussed in Sec. III B, this nonzero cross term corresponds to a tilt in the $q_{\rm out}$-$q_{\rm long}$ plane. The nonzero value of the cross term means there is a correlation between the relative momentum of particle pairs in the out and long directions.

Two considerations affect how $R^2_{ol,0}$ (or any of the radii) are related to physical parameters of interest. One is the frame in which the correlation function is constructed (fixed center of mass, LCMS, etc.) [52,80]. The other involves the assumptions that enter a particular analytical model of the source distribution (static, longitudinal flow, transverse flow, boost-invariance, etc.) that is required to relate the extracted fit parameters (radii) to physical quantities such as freeze-out duration or total lifetime [52,80].

Assume for the moment that radii are measured in the LCMS frame, as in this analysis. In models with longitudinal expansion, breaking of boost-invariance results in nonzero values of the $R^2_{ol,0}$ cross term away from midrapidity [52,80].

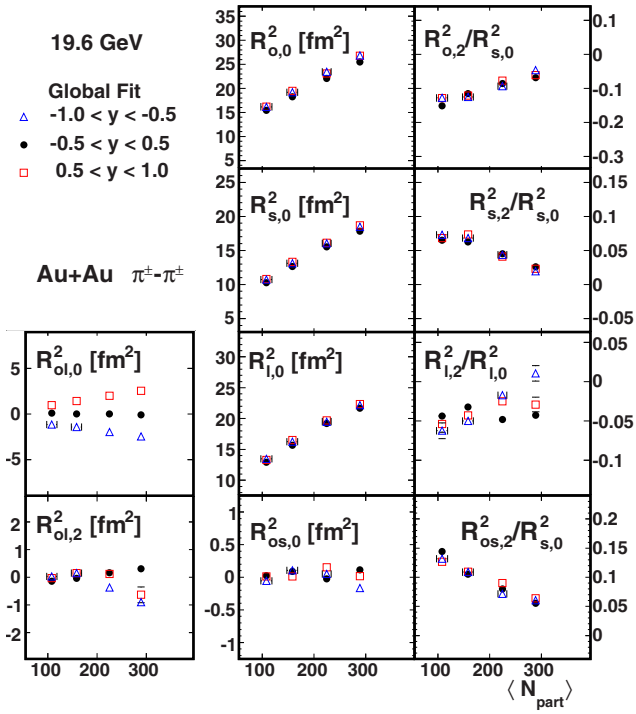

FIG. 17. (Color online) Centrality dependence of the Fourier coefficients that describe azimuthal oscillations of the HBT radii, at backward ($-1 < y < -0.5$), forward ($0.5 < y < 1$), and mid-($-0.5 < y < 0.5$) rapidity, in 19.6-GeV collisions with $\langle k_T \rangle \approx 0.31$ GeV/c using the global fit method. Error bars include only statistical uncertainties. The 0%–5% global fit point is excluded.

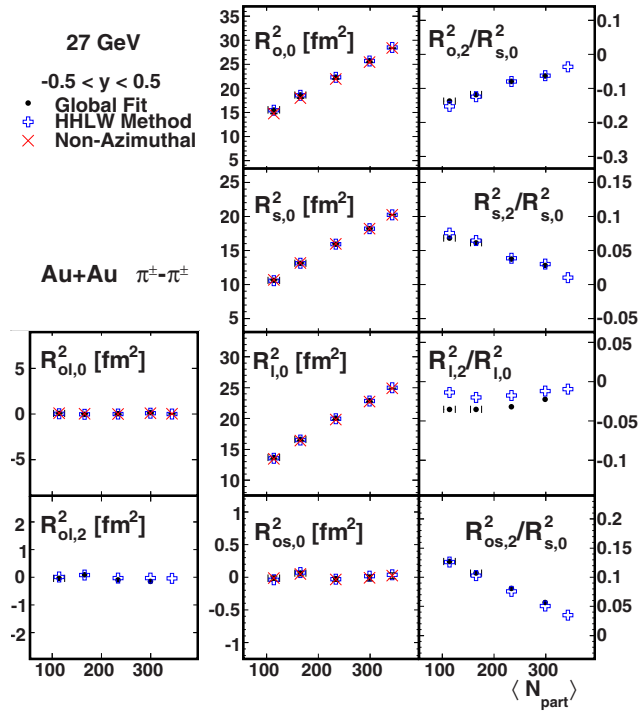

FIG. 18. (Color online) Centrality dependence of the Fourier coefficients that describe azimuthal oscillations of the HBT radii, at midrapidity ($-0.5 < y < 0.5$), in 27-GeV collisions with $\langle k_T \rangle \approx 0.31$ GeV/c. The symbols have the same meaning as in Fig. 12. Error bars include only statistical uncertainties. The 0%–5% global fit method point is excluded.

The reason is that the LCMS and local rest frame of the source only coincide in the boost-invariant model [80]. This is one example of how changing the model assumptions leads to a different relationship between the radii (including $R^2_{\mathrm{ol},0}$) and physical parameters.

Alternatively, if the same analytical model is assumed but the measurement is performed in different frames, the dependence of the radii on the physical parameters will also change. Reference [80] demonstrates that, assuming boost invariant longitudinal expansion, measurement in a fixed frame, the LCMS frame, and a generalized Yano-Koonin frame lead to three different relationships between the fit parameters (radii) and physical quantities. In Ref. [52], a similar analytical model leads to a quite complex dependence of $R^2_{\mathrm{ol},0}$ on various physical quantities in the center-of-mass frame. However, the expression greatly simplifies in the LCMS frame, leaving $R^2_{\mathrm{ol},0}$ directly proportional to the freeze-out duration and other parameters.

Figure 26 shows that, for each centrality, $R^2_{\mathrm{ol},0}$ decreases smoothly toward zero at higher collision energy. It has been suggested [52,80] that the quantity $R^2_{\mathrm{out}} - R^2_{\mathrm{side}}$ is sensitive to the duration of particle emission, $\Delta\tau$, which provided the main motivation for the past studies of $R_{\mathrm{out}}/R_{\mathrm{side}}$, summarized in Fig. 6. The R^2_{ol} offset has also been associated with the duration of freeze-out and other parameters in a mathematically different way [52,80]. Within the framework of a given model, these new data may allow an estimate of $\Delta\tau$ (and also other parameters described in the references) as a function of beam energy, using a variable that has different dependence on $\Delta\tau$ than does the more commonly studied quantity $R^2_{\mathrm{out}} - R^2_{\mathrm{side}}$.

One other observation can be made because the $R^2_{\mathrm{ol},0}$ values in Fig. 26 are measured in the LCMS frame. As mentioned above, nonzero values of $R^2_{\mathrm{ol},0}$ suggest boost invariance may be broken. The higher absolute values of $R^2_{\mathrm{ol},0}$ at lower $\sqrt{s_{NN}}$ may thus reflect that the assumption of boost-invariance becomes less valid at lower energies.

3. *Kinetic freeze-out eccentricity*

Once the Fourier coefficients are extracted the eccentricity, defined as

$$\varepsilon_F = \frac{\sigma_y'^2 - \sigma_x'^2}{\sigma_y'^2 + \sigma_x'^2} \approx 2\frac{R^2_{\mathrm{s},2}}{R^2_{\mathrm{s},0}}, \tag{20}$$

can be simply computed [23]. The variances σ'_y and σ'_x correspond to the widths of the collision fireball at kinetic freeze-out in the out-of-plane and in-plane directions, respectively. This definition allows negative eccentricities if $\sigma'_y < \sigma'_x$, which would indicate that the system expanded enough to become in-plane extended. Whether or not that happens is related to the collision dynamics and equation of state as described in Sec. II. The ratio $R^2_{\mathrm{s},2}/R^2_{\mathrm{s},0}$ is used to estimate ε_{F} because R_{side} is less affected by flow, and hence it carries primarily geometric information [23].

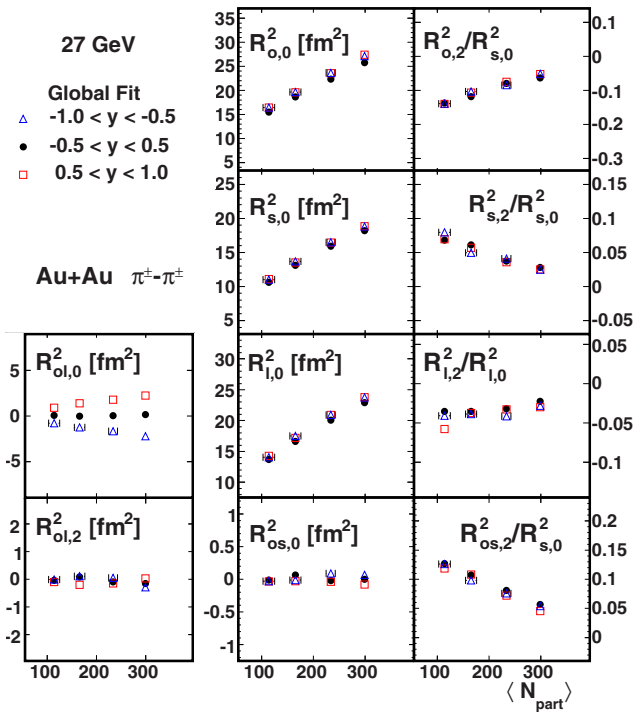

FIG. 19. (Color online) Centrality dependence of the Fourier coefficients that describe azimuthal oscillations of the HBT radii, at backward ($-1 < y < -0.5$), forward ($0.5 < y < 1$), and mid-($-0.5 < y < 0.5$) rapidity, in 27-GeV collisions with $\langle k_T \rangle \approx 0.31$ GeV/c using the global fit method. Error bars include only statistical uncertainties. The 0%–5% global fit point is excluded.

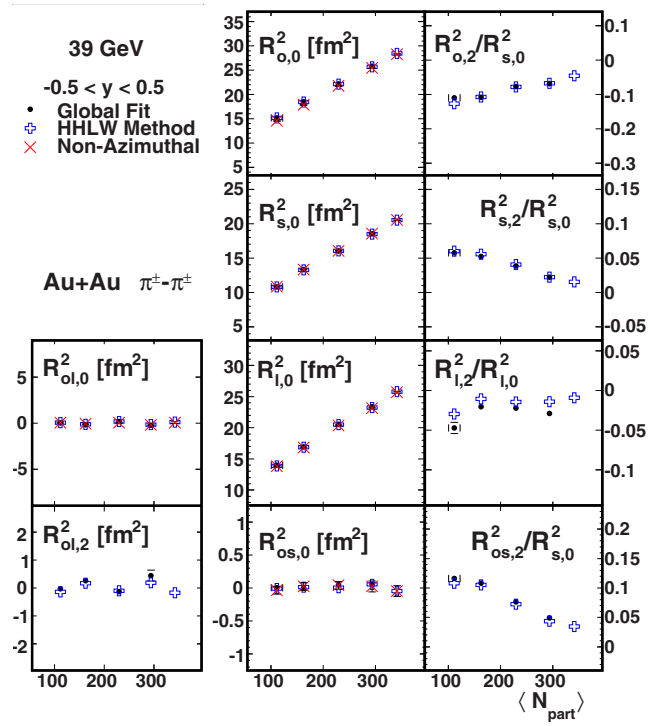

FIG. 20. (Color online) Centrality dependence of the Fourier coefficients that describe azimuthal oscillations of the HBT radii, at midrapidity ($-0.5 < y < 0.5$), in 39-GeV collisions with $\langle k_T \rangle \approx 0.31$ GeV/c. The symbols have the same meaning as in Fig. 12. Error bars include only statistical uncertainties. The 0%–5% global fit method point is excluded.

Figure 27 shows the eccentricities at kinetic freeze-out, ε_F, defined in Eq. (20), for all centralities and energies. They are plotted against the initial eccentricity relative to the participant plane obtained from the Glauber model [49], defined as

$$\varepsilon_{\rm PP} = \frac{\sqrt{\left(\sigma_y^2 - \sigma_x^2\right)^2 + 4\sigma_{xy}^2}}{\sigma_x^2 + \sigma_y^2}. \qquad (21)$$

The variances $\sigma_x^2 = \{x^2\} - \{x\}^2$ and $\sigma_y^2 = \{y^2\} - \{y\}^2$ gauge the widths of the distributions of participant nucleons in and out of the reaction-plane direction, respectively. The symbol $\{\cdots\}$ denotes averaging of participant nucleons, with positions x and y, in each event. The covariance $\sigma_{xy} = \{xy\} - \{x\}\{y\}$ accounts for event-by-event fluctuations in the distribution of participant nucleons. The line has a slope of one ($\varepsilon_F = \varepsilon_{\rm PP}$), so points further below the line have evolved more toward a round shape ($\varepsilon_F = 0$). These results demonstrate that, at all energies studied, the freeze-out shape remains an out-of-plane extended ellipse ($\varepsilon_F > 0$). In no case does extended lifetime or stronger flow result in the shape becoming in-plane extended ($\varepsilon_F < 0$). However, there is always some evolution toward a more round shape, as expected, and there tends to be slightly more evolution for the higher energies. The same observations apply at forward and backward rapidity because of the similar trends observed for the ratio $R_{\rm s,2}^2/R_{\rm s,0}^2$ ($=\varepsilon_F/2$).

The excitation function for the freeze-out shape is presented in Fig. 28. The new STAR results for three rapidities are compared to earlier measurements from other experiments and to several models. The results use the global fit method and are for midperipheral (10%–30%) collisions where the initial anisotropic shape is large but there is still significant overlap of the nuclei. The larger differences between in-plane and out-of-plane pressure gradients in these collisions and larger initial spatial anisotropy could admit more varied results in the change in shape, if that where to happen at different energies. The new STAR results exhibit a monotonic decrease in the freeze-out eccentricity with increasing beam energy for all three rapidity regions.

The freeze-out eccentricity values from CERES and STAR at similar energy and centrality are not consistent. There are some differences in analyses from these different experiments such as correction for event-plane resolution, fitting in one k_T bin versus averaging several smaller k_T bins, and centrality ranges. These could potentially be important and were studied. The CERES point at 17.3 GeV suggested a possible minimum in the historical data. The new STAR results at 11.5 and 19.6 GeV at midrapidity were significantly higher, suggesting a monotonic decrease in the freeze-out shape. To check that the difference was not attributable to the different rapidity windows the STAR analysis was extended to include the same rapidity region as CERES, $0.5 < |y| < 1$. The forward and backward rapidity results remained consistent with the midrapidity measurement. The CERES point for 10%–25% centrality is consistent with the (smaller) eccentricities for

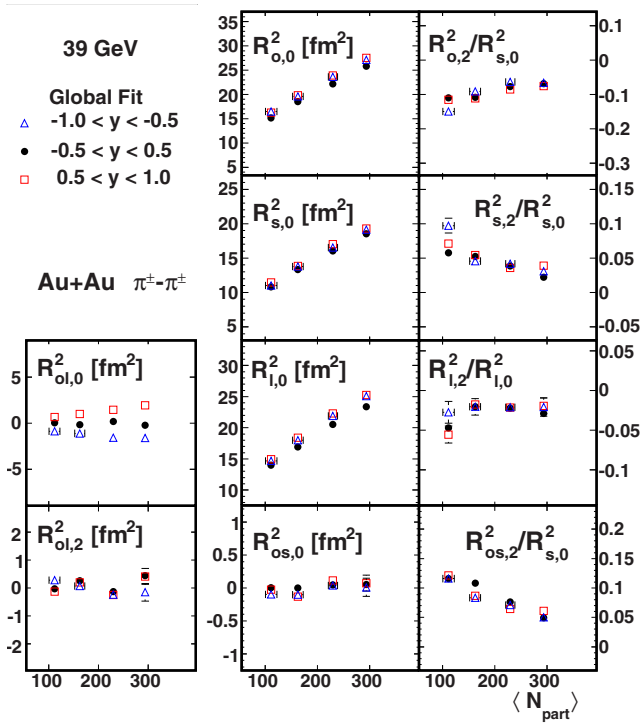

FIG. 21. (Color online) Centrality dependence of the Fourier coefficients that describe azimuthal oscillations of the HBT radii, at backward ($-1 < y < -0.5$), forward ($0.5 < y < 1$), and mid-($-0.5 < y < 0.5$) rapidity, in 39-GeV collisions with $\langle k_T \rangle \approx 0.31$ GeV/c using the global fit method. Error bars include only statistical uncertainties. The 0%–5% global fit point is excluded.

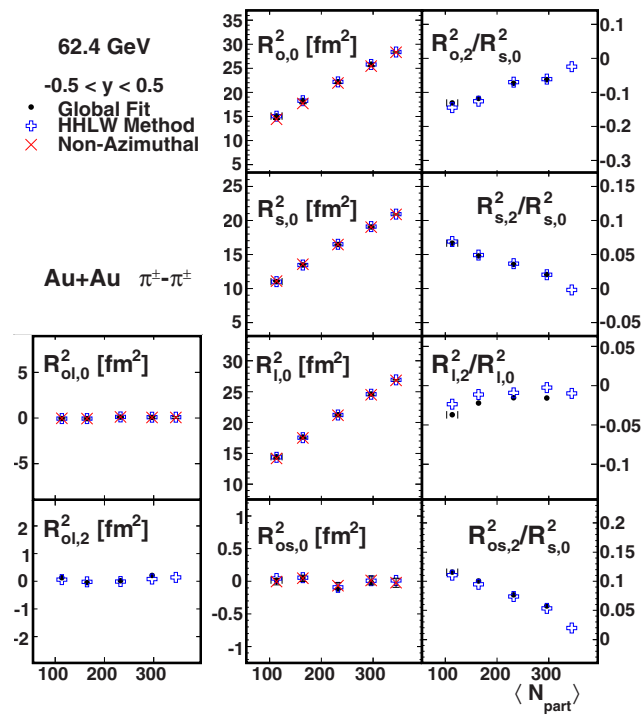

FIG. 22. (Color online) Centrality dependence of the Fourier coefficients that describe azimuthal oscillations of the HBT radii, at midrapidity ($-0.5 < y < 0.5$), in 62.4-GeV collisions with $\langle k_T \rangle \approx 0.31$ GeV/c. The symbols have the same meaning as in Fig. 12. Error bars include only statistical uncertainties. The 0%–5% global fit method point is excluded.

the 0%–5% and 5%–10% centrality ranges in STAR results at 19.6 GeV, so it seems rather unlikely that large-enough differences in centrality definitions could occur to cause such a large difference in the eccentricities for STAR and CERES. Event, track, and pair selection quantities have rather little effect on the results. Another difference is the range of k_T values included in the fits. In the CERES and earlier STAR result [40], the azimuthal analysis was done in narrow k_T bins and the ε_F values averaged. This was problematic at the lowest energies owing to lower statistics when the analysis was additionally differential in k_T. Using a single, wide k_T bin biases the results slightly toward smaller ε_F values, as discussed in Sec. III D. Therefore, to be consistent, the same (wide k_T bin) method is used for all the STAR points. The CERES results used a weighted average of results in narrow k_T bins which should be equivalent to using a single, wide k_T bin. It seems unlikely that this is the cause of the discrepancy. The E895 correction algorithm was used in the CERES and E895 cases to correct for the event-plane resolution while in the STAR case the histograms were corrected or the fit function smeared in the global fit case. The difference in the results is rather tiny for these different methods and also cannot explain the difference.

As discussed in Sec. II, nonmonotonic behavior in the excitation function would have strongly suggested interesting changes in the equation of state. The observed monotonic decrease excludes the scenario described in Ref. [19] and is consistent with increased lifetime and/or pressure gradients at higher energy. The energy dependence of $R_{\rm long}$ from the nonazimuthal analysis, and the lifetimes shown in Fig. 11, suggest also that the system is longer-lived at higher energy. Still, these results will make it possible to probe equation of state effects by comparing to various models.

The currently available model predictions [19,45,81] for the energy dependence of the freeze-out eccentricity are also shown in Fig. 28. All models predict a monotonic decrease in the freeze-out shape at higher energies similar to the data. The older $(2+1)$-dimensional, ideal hydrodynamical models [45], labeled EOS-H, EOS-I, and EOS-Q, all overpredict the data. As was noted in Ref. [81], in comparison to the historical data, the model with a first-order phase transition, EOS-Q, gets close to the 200-GeV point. The predictions of the freeze-out shape are sensitive to the equation of state used in the hydrodynamic models. This is clear by comparing the curves for EOS-I (ideal, massless quark gluon gas) and EOS-H (hadronic gas). For EOS-Q, the slope changes, following EOS-H at low energies, but dropping more rapidly at higher energies. This is attributed to passage through a mixed-phase regime which extends the lifetime, allowing the system to evolve to a more round state at higher energies [19].

The two more recent $(2+1)$-dimensional predictions, from the VISH2 + 1 model, get closer to the data. MC-KLN and MC-GLB correspond to different initial conditions and are more realistic than the earlier results as they make it possible

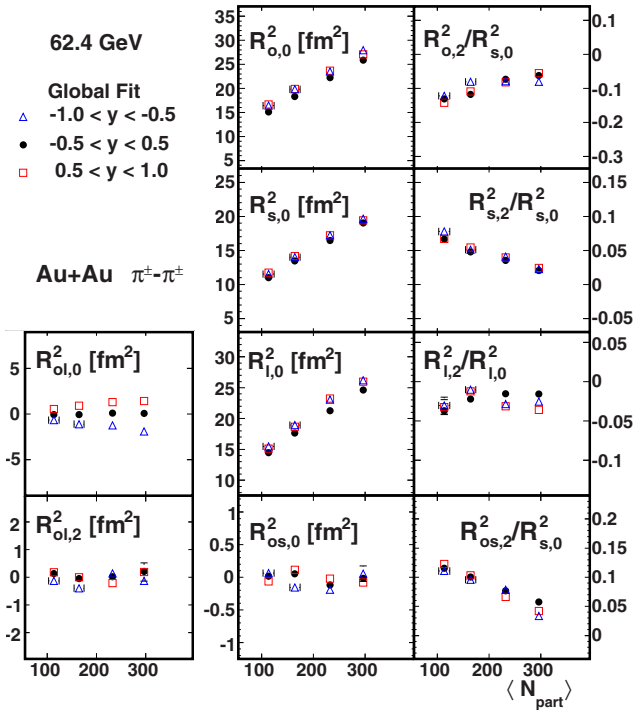

FIG. 23. (Color online) Centrality dependence of the Fourier coefficients that describe azimuthal oscillations of the HBT radii, at backward ($-1 < y < -0.5$), forward ($0.5 < y < 1$) and mid ($-0.5 < y < 0.5$) rapidity, in 62.4 GeV collisions with $\langle k_T \rangle \approx 0.31$ GeV/c using the global fit method. Error bars include only statistical uncertainties. The 0%–5% global fit point is excluded.

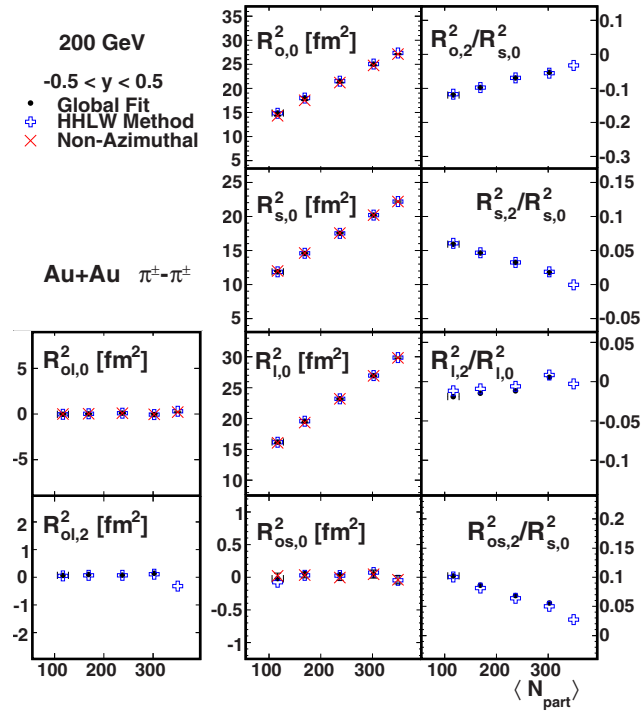

FIG. 24. (Color online) Centrality dependence of the Fourier coefficients that describe azimuthal oscillations of the HBT radii, at midrapidity ($-0.5 < y < 0.5$), in 200-GeV collisions with $\langle k_T \rangle \approx 0.31$ GeV/c. The symbols have the same meaning as in Fig. 12. Error bars include only statistical uncertainties. The 0%–5% global fit method point is excluded.

to incorporate viscous effects [81]. MC-GLB uses a specific shear viscosity of $\eta/s = 0.08$ with Glauber initial conditions. The MC-KLN model has a much larger specific shear viscosity, $\eta/s = 0.2$, and the initial shape is derived from the initial gluon density distribution in the transverse plane (which is converted to an entropy and, finally, energy density profile). Both models incorporate an equation of state based on lattice QCD, named s95p-PCE [82,83]. Initial parameters in the models were calibrated using measured multiplicity distributions (and extrapolations to lower energies) and to describe p_T spectra and v_2 measurements for 200 GeV Au + Au collisions at RHIC. The two cases were found to yield similar lifetimes, but in the MC-KLN case the initial eccentricities are larger (more out-of-plane extended). The MC-KLN model achieves a less round shape simply because it starts with larger initial eccentricity [81]. The excitation function for freeze-out eccentricities has the potential to resolve ambiguities between models with different initial conditions and values of η/s. In particular, the two sets of initial conditions and η/s used here yield identical v_2, but very different ε_F. So the results in Fig. 28 provide tighter constraints on these models.

The goal of Ref. [81] was to map systematic trends in observables with the two models, not to explain the data precisely. In fact, the applicability of these models is known to be problematic at lower energies both because they assume boost-invariance, which is broken at lower energy, and because the hadronic phase is expected to become more important at lower collision energy. A more realistic calculation requires (3 + 1)-dimensional viscous hydrodynamics. Nevertheless, the new calculations are able to match more closely the experimental results. Of the hydrodynamical models, MC-GLB is closest to the data although it still overpredicts the freeze-out eccentricity and the slope appears too steep. One relevant observation from Ref. [81] is that in these models the decrease in the eccentricity with energy appears to be due mainly to an extended lifetime rather than larger anisotropy of pressure gradients. As discussed at the end of Sec. VI A, the lifetime extracted from $R_{\rm long}$ values also suggest an increase in the total lifetime. However, the data cannot allow one to determine whether the decrease in eccentricity is due solely to increased lifetime or whether the pressure gradients may also play a significant role.

The prediction of the Boltzmann transport model, UrQMD (v2.3) [84], matches most closely the freeze-out shape at all energies [19]. UrQMD follows the trajectories and interactions of all hadronic particles throughout the collision, so it does not require assumptions about how freeze-out occurs. The model is three-dimensional and does not require boost invariance; therefore, it is equally applicable at all the studied energies. This may be, at least partially, why the predictions from UrQMD more closely match the energy dependence of the data compared to the hydrodynamic predictions. While it does not explicitly contain a deconfined state, it does incorporate color degrees of freedom through inclusion of the creation of color strings and their subsequent decay back into hadrons.

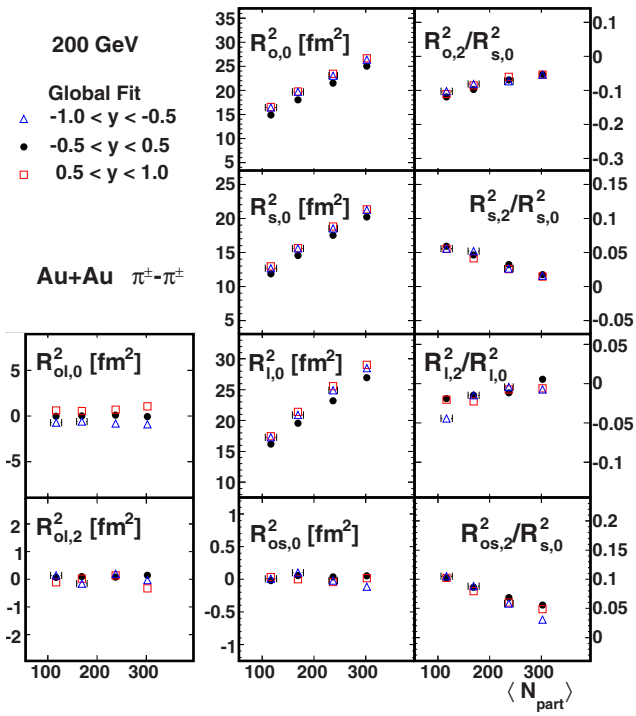

FIG. 25. (Color online) Centrality dependence of the Fourier coefficients that describe azimuthal oscillations of the HBT radii, at backward ($-1 < y < -0.5$), forward ($0.5 < y < 1$), and mid-($-0.5 < y < 0.5$) rapidity, in 200-GeV collisions with $\langle k_T \rangle \approx 0.31$ GeV/c using the global fit method. Error bars include only statistical uncertainties. The 0%–5% global fit point is excluded.

For the azimuthally integrated results, UrQMD does rather well at predicting the observed dependence of HBT radii on $\langle k_T \rangle$ and centrality [85,86]. As discussed earlier, inclusion of a mean field acting between preformed hadrons (color string fragments) predicts $R_{\rm out}/R_{\rm side}$ ratios similar to the observed values and leads naturally to a minimum in the volume similar

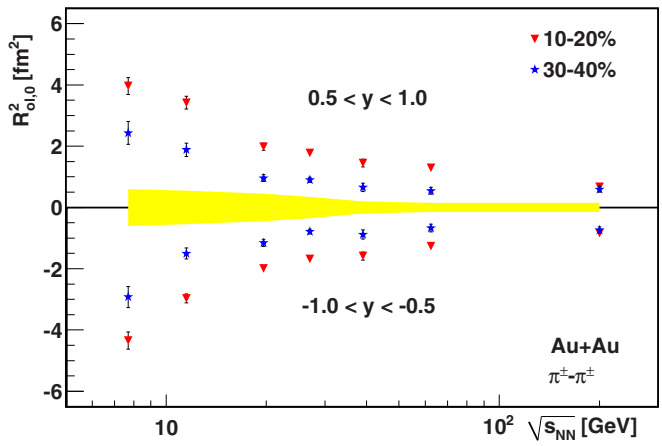

FIG. 26. (Color online) Beam energy dependence of the $R^2_{\rm ol,0}$ cross term for forward and backward rapidity with $\langle k_T \rangle \approx 0.31$ GeV/c. The yellow band shows estimated systematic uncertainty.

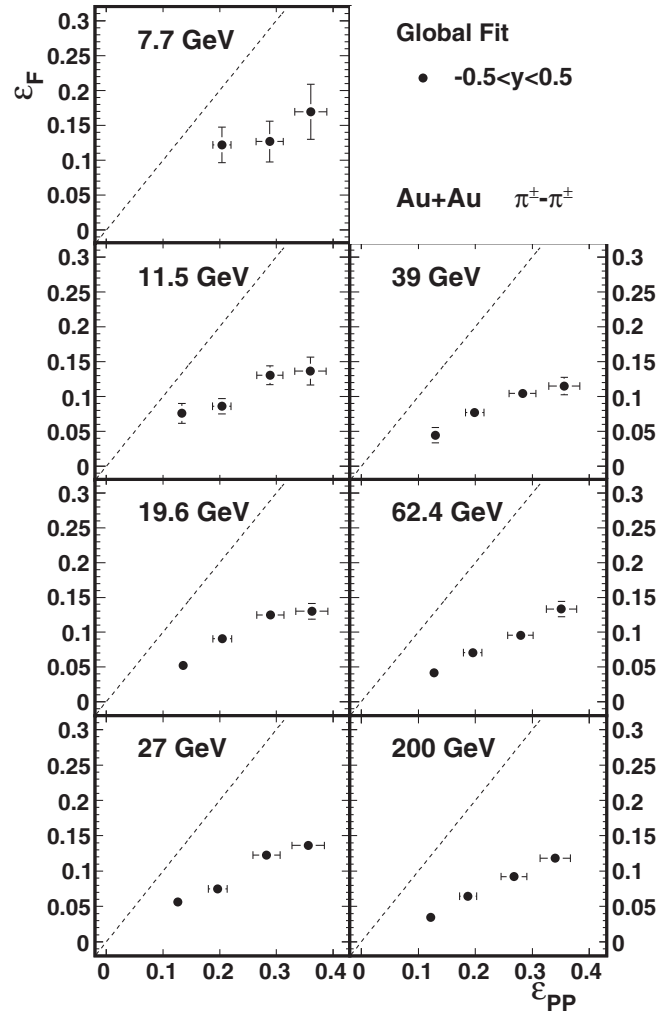

FIG. 27. The eccentricity of the collisions at kinetic freeze-out, $\varepsilon_{\rm F}$, as a function of initial eccentricity relative to the participant plane, $\varepsilon_{\rm PP}$, at midrapidity. All results are for $\langle k_T \rangle \approx 0.31$ GeV/c. Error bars include only statistical uncertainties. The line has a slope of 1, indicating no change in shape. Points further below the line evolve more to a round shape.

to that which is observed experimentally [78,79]. Such a repulsive potential between the string fragments would mimic somewhat an increase in pressure gradients at early stages [79] similar to the hydrodynamics cases with an equation of state that includes a phase transition. The UrQMD predictions for the eccentricities at kinetic freeze-out in Fig. 28 were made with UrQMD in cascade mode and so do not incorporate this potential between string fragments.

It should be noted that none of the models predict all observables simultaneously. The UrQMD model, while it matches the freeze-out shapes well, matches the momentum-space observables less well [70,87]. The hydrodynamic models, while they are able to describe the momentum space p_T spectra and v_2 results, do less well at predicting the eccentricity and trends observed in HBT analyses [22,81]. The availability of these new experimental results provide an important opportunity to further constrain models.

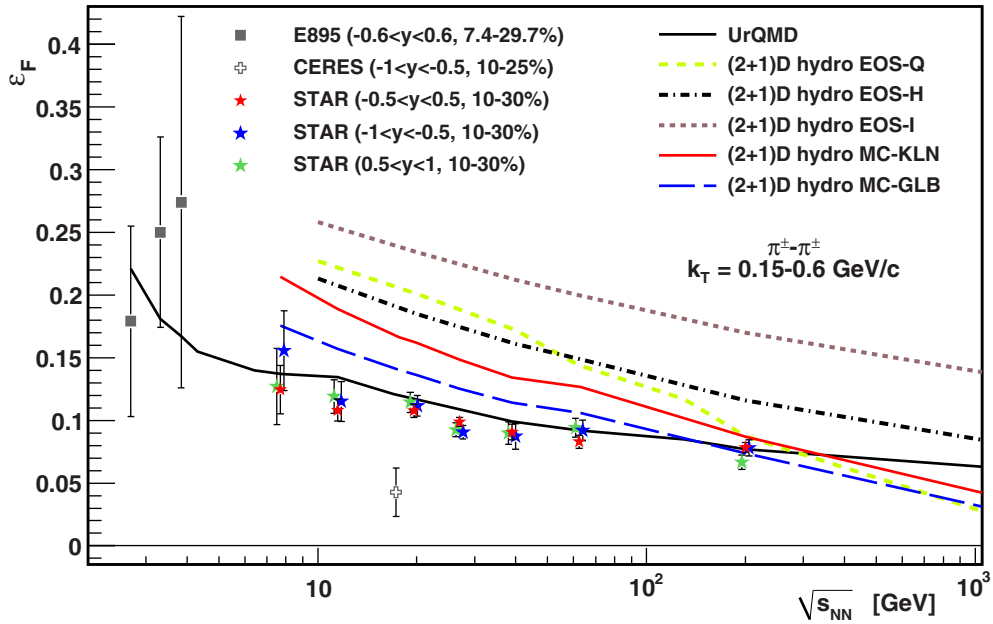

FIG. 28. (Color online) The dependence of the kinetic freeze-out eccentricity of pions on collision energy in midcentral Au + Au collisions (E895, STAR) and Pb + Au collisions (CERES) for three rapidity regions and with $\langle k_T \rangle \approx 0.31$ GeV/c. For clarity, the points for forward and backward rapidity from STAR are offset slightly. Error bars include only statistical uncertainties. Several (2 + 1)-dimensional hydrodynamical models and UrQMD calculations are shown. Model centralities correspond to the data. The trend is consistent with a monotonic decrease in eccentricity with beam energy. Systematic measurement uncertainty on ϵ is about the size of the data points (0.005) and independent of $\sqrt{s_{NN}}$. This systematic uncertainty is significantly smaller than statistical uncertainties and so is not drawn, to reduce clutter.

VII. CONCLUSIONS

The two-pion HBT analyses that have been presented provide key measurements in the search for the onset of a first-order phase transition in Au + Au collisions as the collision energy is lowered. The Beam Energy Scan program has allowed HBT measurements to be carried out across a wide range of energies with a single detector and identical analysis techniques. In addition to standard azimuthally integrated measurements, we have performed comprehensive, high-precision, azimuthally sensitive femtoscopic measurements of like-sign pions. To obtain the most reliable estimates of the eccentricity of the collisions at kinetic freeze-out, a new global fit method has been developed.

A wide variety of HBT measurements have been performed and the comparison of results at different energies is greatly improved. In the azimuthally integrated case, the beam energy dependence of the radii generally agree with results from other experiments, but show a much smoother trend than the earlier data, which were extracted from a variety of experiments with variations in analysis techniques. The current analyses additionally contribute data in previously unexplored regions of collision energy. The transverse mass dependence is also consistent with earlier observations and allows one to conclude that all k_T and centrality bins exhibit similar trends as a function of collision energy.

The energy dependence of the volume of the homogeneity regions is consistent with a constant mean free path at freeze-out, as is the very flat energy dependence of $R_{\rm out}$. This scenario also explains the common dependence of $R_{\rm side}$ and $R_{\rm long}$ on the cube root of the multiplicity that is observed at higher energy. For 7.7 and 11.5 GeV, $R_{\rm side}$ appears to deviate slightly from the trend at the higher energies. Two physical changes that may potentially be related to this are the effects of strangeness enhancement (not included in the argument for a constant mean free path at freeze-out) and the rapid increase in the strength of v_2 that levels off around 7.7 to 11.5 GeV. Both of these physical changes occur in the vicinity of the minimum. A systematic study with a single detector at slightly lower energies would be needed to help disentangle the different effects.

The UrQMD model provides an alternative explanation for the minimum in the volume measurement in terms of a change from a hadronic to a partonic state. Including interactions between color string fragments early in the collision, it not only can explain the minimum in the volume, but is also able to find $R_{\rm out}/R_{\rm side}$ values close to unity as observed from AGS through RHIC energies and improves the agreement between UrQMD and other observables at the same time. It is interesting that such an interaction potential may somewhat mimic an increase in the pressure gradients, which may correlate with the observation that v_2 increases rapidly with $\sqrt{s_{NN}}$ in this region also.

The lifetime of the collision evolution was extracted using the $\langle m_T \rangle$ dependence of $R_{\rm long}$. Subject to certain assumptions, the lifetime increases by a factor 1.7 from AGS to 200-GeV collisions measured at STAR. The lifetime increases by about 1.4 times more between RHIC and the LHC. The magnitude of the increased lifetime effect is well beyond systematic measurement uncertainties.

A new global fit method was developed and studied in relation to the HHLW fit method. For most centralities, this

method is found to yield more reliable results in cases of low statistics and poor event-plane resolution, although it has problems in the most central bin related to different parametrizations. As discussed in Sec. V C, the global fit has the additional benefit that each q bin for all correlation functions is used precisely once in the fit to extract the parameters $R^2_{\mu,n}$. This eliminates issues with correlated errors that arise when q bins from correlation functions at all Φ values are used to correct for reaction-plane resolution in the HHLW approach. This global fit method has allowed the extraction of the most reliable results at the lowest energies studied.

The Fourier coefficients measured away from midrapidity allow one to extract the energy dependence of the $R^2_{\mathrm{ol},0}$ cross term. This previously unavailable observable exhibits a monotonic decrease as a function of beam energy. This observable has been connected to the duration of particle emission in a way that is different than the more commonly studied quantities $R^2_{\mathrm{out}} - R^2_{\mathrm{side}}$ or $R_{\mathrm{out}}/R_{\mathrm{side}}$. This measurement may provide constraints for models that relate the radii and physical quantities with different sets of assumptions.

The azimuthally differential results show that, for all energies, the system remains out of plane extended at freeze-out, despite the evolution of the collision eccentricity. In midcentral (10%–30%) collisions, the freeze-out eccentricity shows a monotonic decrease with beam energy consistent with expectations of increased flow and/or increased lifetime at higher energies. This is supported by the azimuthally integrated results which suggest longer lifetimes at higher energies. The results are consistent qualitatively with the monotonic decrease suggested by all model predictions, but is most consistent quantitatively with UrQMD. While the hydrodynamic models can match momentum-space observables (p_T spectra, v_2) well, they do less well at predicting the HBT results. At the same time, while the UrQMD model does better at predicting the HBT results, like the freeze-out shape, it does less well at predicting the momentum-space observables. The freeze-out eccentricity excitation function provides new, additional information that will help to constrain future model investigations.

ACKNOWLEDGMENTS

We thank the RHIC Operations Group and RCF at BNL, the NERSC Center at LBNL, the KISTI Center in Korea, and the Open Science Grid consortium for providing resources and support. This work was supported in part by the Offices of NP and HEP within the US DOE Office of Science, the US NSF, CNRS/IN2P3; FAPESP CNPq of Brazil; Ministry of Education and Science of the Russian Federation; NNSFC, CAS, MoST, and MoE of China; the Korean Research Foundation; GA and MSMT of the Czech Republic; FIAS of Germany; DAE, DST, and CSIR of India; National Science Centre of Poland; National Research Foundation of the Republic of Croatia, Ministry of Science, Education and Sports of the Republic of Croatia; and RosAtom of Russia.

APPENDIX: NON-GAUSSIAN EFFECTS ON AZIMUTHAL HBT ANALYSES

In azimuthally integrated HBT analyses, the cross terms (R_{os}, R_{ol}, R_{sl}) vanish at midrapidity. In this case, the sign of the components of the relative momentum vector, $\vec{q}$, are arbitrary. The three-dimensional $\vec{q}$-space distributions (numerator, denominator, and Coulomb weighted distributions) may be folded, so that q_{long} and q_{side} are always positive, for instance, to increase statistics in each (q_{out}, q_{side}, q_{long}) bin. In azimuthally differential analyses, however, the relative signs of components are important to extract nonzero cross terms [33,88]. At midrapidity, the relative sign of q_{out} and q_{side} must thus be maintained to extract values of R^2_{os}. Away from midrapidity, the R^2_{ol} cross term is also nonzero and q_{long} must be allowed to have both positive or negative values. This way the relative sign of q_{out} and q_{long} is maintained and the corresponding cross term can be extracted.

If the "q-folding" procedure is performed and the cross terms are included as fit parameters, the fit parameters become strongly correlated and the values of the extracted radii change. The size of this effect varies randomly from one azimuthal bin to the next, causing large variations in the extracted oscillations of the radii. This behavior is related to the non-Gaussianness of the correlation function. Owing to the necessity of using finite bins in k_T and centrality, which are described by a range of radii, the radii extracted from these correlation functions are some average value. If too much q folding is performed, the signs of the relative momentum components are lost. In cases where the cross terms associated with these relative momentum components are nonzero, the covariance of fit parameters that appears allows deviations from the average values and the results become unreliable.

This is an important consideration for any HBT analysis performed away from mid-rapidity, or relative to the first-order reaction plane, where measurement of cross terms is important. In this analysis, no folding of $\vec{q}$ space is performed and so any possible effects of this phenomena are eliminated.

[1] M. M. Aggarwal *et al.* (STAR Collaboration) , arXiv:1007.2613.
[2] J. Adams *et al.* (STAR Collaboration), Nucl. Phys. A **757**, 102 (2005).
[3] K. Adcox *et al.* (PHENIX Collaboration), Nucl. Phys. A **757**, 184 (2005).
[4] B. B. Back *et al.* (PHOBOS Collaboration), Nucl. Phys. A **757**, 28 (2005).
[5] I. Arsene *et al.* (BRAHMS Collaboration), Nucl. Phys. A **757**, 1 (2005).
[6] F. R. Brown, F. P. Butler, H. Chen, N. H. Christ, Z. Dong, W. Schaffer, L. I. Unger, and A. Vaccarino, Phys. Rev. Lett. **65**, 2491 (1990).
[7] Y. Aoki, G. Endrodi, Z. Fodor, S. Katz, and K. Szabo, Nature (London) **443**, 675 (2006).

[8] S. Borsanyi *et al.* (Wuppertal-Budapest Collaboration), J. High Energy Phys. 09 (2010) 073.
[9] M. Cheng (HotQCD Collaboration), PoS **LAT2009**, 175 (2009).
[10] A. Masayuki and Y. Koichi, Nucl. Phys. A **504**, 668 (1989).
[11] A. Barducci, R. Casalbuoni, G. Pettini, and R. Gatto, Phys. Rev. D **49**, 426 (1994).
[12] J. Berges and K. Rajagopal, Nucl. Phys. B **538**, 215 (1999).
[13] M. A. Halasz, A. D. Jackson, R. E. Shrock, M. A. Stephanov, and J. J. M. Verbaarschot, Phys. Rev. D **58**, 096007 (1998).
[14] O. Scavenius, A. Mócsy, I. N. Mishustin, and D. H. Rischke, Phys. Rev. C **64**, 045202 (2001).
[15] N. G. Antoniou and A. S. Kapoyannis, Phys. Lett. B **563**, 165 (2003).
[16] Y. Hatta and T. Ikeda, Phys. Rev. D **67**, 014028 (2003).
[17] M. Stephanov, Prog. Theor. Phys. Suppl. **153**, 139 (2004).
[18] J. Randrup, Phys. Rev. C **82**, 034902 (2010).
[19] M. A. Lisa, E. Frodermann, G. Graef, M. Mitrovski, E. Mount, H. Petersen, and M. Bleicher, New J. Phys. **13**, 065006 (2011).
[20] R. H. Brown and R. Q. Twiss, Nature (London) **178**, 1046 (1956).
[21] G. Goldhaber, S. Goldhaber, W. Lee, and A. Pais, Phys. Rev. **120**, 300 (1960).
[22] M. A. Lisa, S. Pratt, R. Soltz, and U. Wiedemann, Annu. Rev. Nucl. Part. Sci. **55**, 357 (2005).
[23] F. Retière and M. A. Lisa, Phys. Rev. C **70**, 044907 (2004).
[24] E. Mount, G. Graef, M. Mitrovski, M. Bleicher, and M. A. Lisa, Phys. Rev. C **84**, 014908 (2011).
[25] L. Ahle *et al.* (E-802 Collaboration), Phys. Rev. C **66**, 054906 (2002).
[26] M. A. Lisa *et al.* (E895 Collaboration), Phys. Rev. Lett. **84**, 2798 (2000).
[27] R. A. Soltz, M. Baker, and J. H. Lee (E866 Collaboration), Nucl. Phys. A **661**, 439 (1999).
[28] D. Adamová *et al.* (CERES Collaboration), Nucl. Phys. A **714**, 124 (2003).
[29] I. G. Bearden *et al.* (NA44 Collaboration), Phys. Rev. C **58**, 1656 (1998).
[30] C. Alt *et al.* (NA49 Collaboration), Phys. Rev. C **77**, 064908 (2008).
[31] M. M. Aggarwal *et al.* (WA98 Collaboration), Phys. Rev. C **67**, 014906 (2003).
[32] B. B. Back *et al.* (PHOBOS Collaboration), Phys. Rev. C **73**, 031901 (2006).
[33] J. Adams *et al.* (STAR Collaboration), Phys. Rev. C **71**, 044906 (2005).
[34] B. I. Abelev *et al.* (STAR Collaboration), Phys. Rev. C **80**, 024905 (2009).
[35] M. M. Aggarwal *et al.* (STAR Collaboration), Phys. Rev. C **83**, 064905 (2011).
[36] K. Aamodt *et al.* (ALICE Collaboration), Phys. Lett. B **696**, 328 (2011).
[37] A. Kisiel (ALICE Collaboration), J. Phys. G **38**, 124008 (2011).
[38] J. L. Gramling (ALICE Collaboration), AIP Conf. Proc. **1422**, 68 (2012).
[39] M. A. Lisa *et al.* (E895 Collaboration), Phys. Lett. B **496**, 1 (2000).
[40] J. Adams *et al.* (STAR Collaboration), Phys. Rev. Lett. **93**, 012301 (2004).
[41] A. Adare *et al.* (PHENIX Collaboration), Phys. Rev. Lett. **112**, 222301 (2014).
[42] D. Adamová *et al.* (CERES Collaboration), Phys. Rev. C **78**, 064901 (2008).
[43] B. Alver and G. Roland, Phys. Rev. C **81**, 054905 (2010).
[44] C. M. Hung and E. V. Shuryak, Phys. Rev. Lett. **75**, 4003 (1995).
[45] P. F. Kolb and U. W. Heinz, in *Quark Gluon Plasma 3*, edited by R. C. Hwa and X.-N. Wang (World Scientific, Singapore, 2004), pp. 634–714, arXiv:nucl-th/0305084.
[46] K. H. Ackermann *et al.* (STAR Collaboration), Nucl. Instrum. Methods A **499**, 624 (2003).
[47] M. Anderson *et al.* (STAR Collaboration), Nucl. Instrum. Methods A **499**, 659 (2003).
[48] K. H. Ackermann *et al.*, Nucl. Phys. A **661**, 681 (1999).
[49] L. Adamczyk *et al.* (STAR Collaboration), Phys. Rev. C **86**, 054908 (2012).
[50] S. Pratt, Phys. Rev. D **33**, 1314 (1986).
[51] G. Bertsch, M. Gong, and M. Tohyama, Phys. Rev. C **37**, 1896 (1988).
[52] S. Chapman, P. Scotto, and U. Heinz, Phys. Rev. Lett. **74**, 4400 (1995).
[53] U. Heinz, A. Hummel, M. A. Lisa, and U. A. Wiedemann, Phys. Rev. C **66**, 044903 (2002).
[54] M. G. Bowler, Phys. Lett. B **270**, 69 (1991).
[55] Y. M. Sinyukov, R. Lednicky, S. Akkelin, J. Pluta, and B. Erazmus, Phys. Lett. B **432**, 248 (1998).
[56] W. A. Zajc *et al.*, Phys. Rev. C **29**, 2173 (1984).
[57] H. W. Barz, Phys. Rev. C **59**, 2214 (1999).
[58] A. M. Poskanzer and S. A. Voloshin, Phys. Rev. C **58**, 1671 (1998).
[59] J. Barrette *et al.* (E877 Collaboration), Phys. Rev. C **55**, 1420 (1997).
[60] H. Appelshäuser *et al.* (NA49 Collaboration), Phys. Rev. Lett. **80**, 4136 (1998).
[61] P. Danielewicz *et al.*, Phys. Rev. C **38**, 120 (1988).
[62] J. Barrette *et al.*, Phys. Rev. C **56**, 3254 (1997).
[63] D. H. Rischke and M. Gyulassy, Nucl. Phys. A **608**, 479 (1996).
[64] U. W. Heinz and P. F. Kolb, in *Proceedings of the 18th Winter Workshop on Nuclear Dynamics*, edited by R. Bellwied, J. Harris, and W. Bauer (EP Systema, Debrecen, Hungary, 2002), pp. 205–216, arXiv:hep-ph/0204061.
[65] U. W. Heinz, B. Tomasik, U. A. Wiedemann, and Y. F. Wu, Phys. Lett. B **382**, 181 (1996).
[66] A. N. Makhlin and Y. M. Sinyukov, Z. Phys. C **39**, 69 (1988).
[67] S. Soff, S. A. Bass, and A. Dumitru, Phys. Rev. Lett. **86**, 3981 (2001).
[68] We thank Roy Lacey for prompting us to reexamine the transverse radii measured at RHIC and LHC separate from older data.
[69] L. Adamczyk *et al.* (STAR Collaboration), Phys. Rev. Lett. **113**, 052302 (2014).
[70] L. Adamczyk *et al.* (STAR Collaboration), Phys. Rev. Lett. **112**, 162301 (2014).
[71] L. Adamczyk *et al.* (STAR Collaboration), Phys. Rev. Lett. **112**, 032302 (2014).
[72] L. Adamczyk *et al.* (STAR Collaboration), Phys. Rev. Lett. **110**, 142301 (2013).
[73] M. Herrmann and G. F. Bertsch, Phys. Rev. C **51**, 328 (1995).
[74] U. A. Wiedemann, P. Scotto, and U. Heinz, Phys. Rev. C **53**, 918 (1996).
[75] D. Adamová *et al.* (CERES Collaboration), Phys. Rev. Lett. **90**, 022301 (2003).

[76] C. Alt *et al.* (NA49 Collaboration), Phys. Rev. C **77**, 024903 (2008).
[77] K. Aamodt *et al.* (ALICE Collaboration), Phys. Rev. Lett. **105**, 252302 (2010).
[78] Q. Li, C. Shen, and M. Bleicher, Cent. Eur. J. Phys. **10**, 1131 (2012).
[79] Q. Li, M. Bleicher, and H. Stocker, Phys. Lett. B **659**, 525 (2008).
[80] S. Chapman, J. R. Nix, and U. Heinz, Phys. Rev. C **52**, 2694 (1995).
[81] C. Shen and U. Heinz, Phys. Rev. C **85**, 054902 (2012).
[82] C. Shen, U. Heinz, P. Huovinen, and H. Song, Phys. Rev. C **82**, 054904 (2010).
[83] P. Huovinen and P. Petreczky, Nucl. Phys. A **837**, 26 (2010).
[84] H. Petersen, M. Bleicher, S. A. Bass, and H. Stocker, arXiv:0805.0567.
[85] Q. Li, M. Bleicher, and H. Stocker, Phys. Rev. C **73**, 064908 (2006).
[86] Q. Li, M. Bleicher, X. Zhu, and H. Stocker, J. Phys. G **34**, 537 (2007).
[87] L. Adamczyk *et al.* (STAR Collaboration), Phys. Rev. C **88**, 014902 (2013).
[88] R. Wells, Ph.D. thesis, The Ohio State University, 2002.